Neurobiology of Aging 113 (2022) 39–54

Contents lists available at ScienceDirect

Neurobiology of Aging

journal homepage: www.elsevier.com/locate/neuaging.org

Regular article

Apolipoprotein ε4 modifies obesity-related atrophy in the hippocampal formation of cognitively healthy adults

Bethany M. Coad[a], Parisa A. Ghomroudi[a], Rebecca Sims[b], John P. Aggleton[c], Seralynne D. Vann[c], Claudia Metzler-Baddeley[a,*]

[a] *Cardiff University Brain Research Imaging Centre (CUBRIC), School of Psychology, Cardiff University, Maindy Road, Cardiff, UK*
[b] *Psychological Medicine and Clinical Neurosciences, School of Medicine, Cardiff University, Cardiff, UK*
[c] *School of Psychology, Cardiff University, Cardiff, UK*

ARTICLE INFO

Article history:
Received 11 November 2021
Revised 18 January 2022
Accepted 12 February 2022
Available online 18 February 2022

Keywords:
Hippocampal subfields
Aging
APOE
Obesity
Microstructural MRI
Episodic memory

ABSTRACT

Characterizing age- and risk-related hippocampal vulnerabilities may inform about the neural underpinnings of cognitive decline. We studied the impact of three risk-factors, Apolipoprotein (*APOE*)-ε4, a family history of dementia, and central obesity, on the CA1, CA2/3, dentate gyrus and subiculum of 158 cognitively healthy adults (38-71 years). Subfields were labelled with the Automatic Segmentation of Hippocampal Subfields and FreeSurfer (version 6) protocols. Volumetric and microstructural measurements from quantitative magnetization transfer and Neurite Orientation Density and Dispersion Imaging were extracted for each subfield and reduced to three principal components capturing apparent myelin/neurite packing, size/complexity, and metabolism. Aging was associated with an inverse U-shaped curve on myelin/neurite packing and affected all subfields. Obesity led to reductions in myelin/neurite packing and size/complexity regardless of *APOE* and family history of dementia status. However, amongst individuals with a healthy Waist-Hip-Ratio, *APOE* ε4 carriers showed lower size/complexity than non-carriers. Segmentation protocol type did not affect this risk pattern. These findings reveal interactive effects between *APOE* and central obesity on the hippocampal formation of cognitively healthy adults.

1. Introduction

The world's population is aging, creating an increase in age-related health issues, including cognitive decline (Beard et al., 2016). With respect to age-related memory impairments, the hippocampal formation, that is, dentate gyrus (DG), cornu Ammonis (CA) fields, and subiculum, warrants particular attention as it is critically involved in memory processing and is affected early in the progression of Alzheimer's disease (AD). Magnetic resonance imaging (MRI) studies have, for example, shown reductions in total hippocampal volume associated with aging in cognitively healthy individuals (Raz, 2001), while hippocampal atrophy remains one of the supporting diagnostic features of amnestic Mild Cognitive Impairment (aMCI) and AD (de Flores et al., 2015a). The next challenge is to distinguish normal age-related hippocampal changes from potential pathological changes related to genetic and lifestyle risk factors of dementia in pre-symptomatic individuals (Jack et al., 2013). Overall structural volumes may, however, lack sufficient sensitivity for early detection. Instead, multi-parametric quantitative MRI indices may provide an alternate route to detect subtle microstructural changes that, in turn, aid our understanding of both age- and dementia risk-related effects on the hippocampal formation and its subfields (Kodiweera et al., 2016; Metzler-Baddeley et al., 2019a; Metzler-Baddeley et al., 2019b; Nazeri et al., 2015; Wolf et al., 2015).

Here, we studied macro- and microstructural properties of the main subfields of the hippocampal formation, that is, CA1, CA2/3, DG and subiculum, in 158 individuals from the Cardiff Aging and Risk of Dementia Study (CARDS) (38-71 years of age) (Coad et al., 2020; Metzler-Baddeley et al., 2019a; Metzler-Baddeley et al., 2019b; Mole et al., 2020).

The objectives of this study were three-fold: Firstly, to characterize the pattern of age and age-independent dementia risk effects on the hippocampal formation in cognitively healthy adults (Metzler-Baddeley et al., 2019a; Metzler-Baddeley et al., 2019b).

---

* Corresponding author at: Cardiff University Brain Research Imaging Centre (CUBRIC), School of Psychology, Cardiff University, Maindy Road, Cardiff CF24 4HQ, UK. Telephone: +44 (0)29 2087 0705; Fax: +44 (0)29 2087 4000.
E-mail address: Metzler-BaddeleyC@cardiff.ac.uk (C. Metzler-Baddeley).

0197-4580/$ – see front matter © 2022 The Author(s). Published by Elsevier Inc. This is an open access article under the CC BY license (http://creativecommons.org/licenses/by/4.0/)
https://doi.org/10.1016/j.neurobiolaging.2022.02.004

The effects of three established risk factors, that is, carriage of the Apolipoprotein E (*APOE)* ε4 genotype (Angelopoulou et al., 2021; Chai et al., 2021; Feringa and van der Kant, 2021; Koutsodendris et al., 2021; Liu et al., 2013), a positive family history (FH) of dementia in a first-grade relative (Alosco et al., 2014; Donix et al., 2010; Johnson et al., 2014; Tanzi, 2012; Wolf, 2012), and central obesity (Arnoldussen et al., 2014; Beydoun et al., 2008; Chuang et al., 2016; Pedditizi et al., 2016; Xu et al., 2011) and their potential interactions were studied (Metzler-Baddeley et al., 2019a; Metzler-Baddeley et al., 2019b; Mole et al., 2020).

The CA1, CA2/3, DG and subiculum subfields were segmented with two publicly available, automated protocols that make use of T_1- and T_2-weighted hippocampal images: The Bayesian inference labeling methods implemented in FreeSurfer 6.0 (Iglesias et al., 2015) and the Automatic Segmentation of Hippocampal Subfields (ASHS) that utilizes multi-atlas segmentation and machine learning techniques (Yushkevich et al., 2015b). Both protocols have been validated with histopathological evidence in patients with epilepsy (Menzler et al., 2021; Mizutani et al., 2021). Employing both ASHS and FreeSurfer allowed us to assess whether the choice of protocol for the labelling of hippocampal subfields had an impact on the analysis of risk effects (Yushkevich et al., 2015a).

Secondly, to investigate the pattern of age and risk effects not only with volumetric but also with multi-parametric microstructural MRI from diffusion neurite density and dispersion imaging (NODDI) (Zhang et al., 2012) and quantitative magnetization transfer (qMT) (Eng et al., 1991; Henkelman et al., 1993; Henkelman et al., 2001; Sled, 2017). NODDI fits a three-compartment tissue model to multishell diffusion-weighted imaging data, which allows the separation of intra- and extracellular tissue properties (Zhang et al., 2012). This is useful as it enables the differentiation between the packing density of neurites, estimated with the intracellular signal fraction (ICSF), and their spatial organization, measured with the orientation dispersion index (ODI). In addition, the amount of free water in the tissue that may accumulate due to age and neurodegeneration-related atrophy can also be estimated with the isotropic signal fraction (ISOSF). Further, we applied a two-pool model to the qMT data that captured the exchange of magnetization between protons in free water and those bound to macromolecules such as lipids and proteins (Henkelman et al. 1993). This model allows the quantification of the macromolecular proton fraction (MPF) that may capture apparent myelin of neurites (Ceckler et al., 1992; Schmierer et al., 2007) and the forward exchange rate k_f that may reflect tissue metabolism (Giulietti et al., 2012; Harrison et al., 2015). Finally, we quantified the longitudinal relaxation rate R_1 for the estimation of apparent water, lipid/protein, and, to a lesser extent, iron content (Callaghan et al., 2015).

Support for studying neurite properties within the context of aging and neurodegeneration comes from neuropathological evidence suggesting that human aging is associated with a reduction of neocortical dendritic spine density (Dickstein et al., 2013) with accompanying compensatory increases in the dendritic extent of DG granular cells (Flood et al., 1985; Flood et al., 1987). Likewise, recent *in vivo* NODDI studies found age-related reductions in neocortical neurite dispersion (Nazeri et al., 2015) and increases in neurite dispersion of the whole hippocampus (Metzler-Baddeley et al., 2019b; Nazeri et al., 2015). With regards to AD pathology, ODI and ICSF were found sensitive to amyloid and tau pathology in the hippocampus (Colon-Perez et al., 2019) and in white matter in AD animal models (Colgan et al., 2016; Colon-Perez et al., 2019). In addition, k_f reductions were reported in the hippocampus, temporal lobes, parietal cortex and posterior cingulate in people with AD (Giulietti et al., 2012) and T_1 and T_2 relaxometry measurements have been found sensitive to AD pathology in animal and human imaging studies (Knight et al., 2016; Knight et al., 2019; Tang et al., 2018). These observations demonstrate that microstructural indices may provide complementary information to volumetric measurements by capturing neurite density and orientation, macromolecular, and free water-related tissue properties (Callaghan et al., 2015; Giulietti et al., 2012; Harrison et al., 2015). Applying these microstructural measurements may therefore aid our understanding of the biophysical properties underpinning aging and risk (Wolf et al., 2015).

Thirdly, we also explored whether individual differences in hippocampal subfield macro- and microstructure correlated with cognitive functions including episodic memory and spatial navigation, abilities known to rely on hippocampal processes (Brown et al., 2014; Hartley et al., 2005; Hoang et al., 2018; Kyle et al., 2015).

The evidence regarding age-related atrophy in hippocampal subfields remains mixed. Volume reductions have previously been reported for CA1 (Malykhin et al., 2017; Mueller and Weiner, 2009; Raz et al., 2015; Uribe et al., 2018; Wisse et al., 2014), CA2-4 (Daugherty et al., 2016; Malykhin et al., 2017; Mueller and Weiner, 2009; Raz et al., 2015; Wisse et al., 2014), subiculum (de Flores et al., 2015b; La Joie et al., 2010; Malykhin et al., 2017; Wolf et al., 2015) and DG (de Flores et al., 2015b; La Joie et al., 2010) but were not consistently observed across all studies. A recent UK Biobank data analysis found non-linear age-related changes in all subfields of the hippocampal formation (Veldsman et al., 2021). In this study, female *APOE* ε4 homozygotes over the age of 65 years exhibited the largest atrophy across CA1, CA3, CA4, subiculum and presubiculum, suggesting that age and sex modulated the effects of *APOE* (Veldsman et al., 2021) (see also Donix et al., 2010; Dounavi et al., 2020; Kerchner et al., 2014; Mueller et al., 2008; Mueller and Weiner, 2009; Reiter et al., 2017). *APOE* ε4-related volume reductions in the molecular layer of the subiculum and the CA fields were also observed in a middle-aged cohort of cognitively healthy participants, while no effects were present for FH or cardiovascular risk (Dounavi et al., 2020). Furthermore, subiculum and CA1 regions have been proposed to be particularly vulnerable in aMCI and AD (Adler et al., 2018; Khan, et al., 2015; Lindberg et al., 2017) and in asymptomatic individuals with positive amyloid and tau cerebrospinal fluid (CSF) biomarkers (Tardif et al., 2018).

In addition, lifestyle-related factors, such as obesity and sedentary lifestyle, may have adverse effects on the hippocampus. For instance, abdominal visceral fat has been found to be associated with volume reductions (Anan et al., 2010) and increases in free water signal of the whole hippocampal formation (Metzler-Baddeley et al., 2019a). Obesity is related to pro-inflammatory states (Cox et al., 2015) and in rodent models was found to induce microglia activation and reduce long-term potentiation in the hippocampus (Hao et al., 2016). It is increasingly recognized that *APOE* ε4 may interact with obesity to augment disruptions in lipid, glucose, insulin, and immune response metabolism and that such adverse interactions may increase the vulnerability of medial temporal lobe structure to neurodegeneration (Jones and Rebeck, 2018; Mole et al., 2020; Zade et al., 2013). However, the nature of these interactions and their impact on the subfields of the hippocampal formation remain poorly understood and require further elucidation.

It is important to note that three source of inconsistency when subdividing the hippocampal formation stems from different subfield and border segmentation protocols (Yushkevich et al., 2015a). Yushkevich et al. (2015a) compared 21 protocols for labelling hippocampal subfields, including those adopted here. They found considerable differences with regards to the region within each segmentation was performed, the set of the employed anatomical

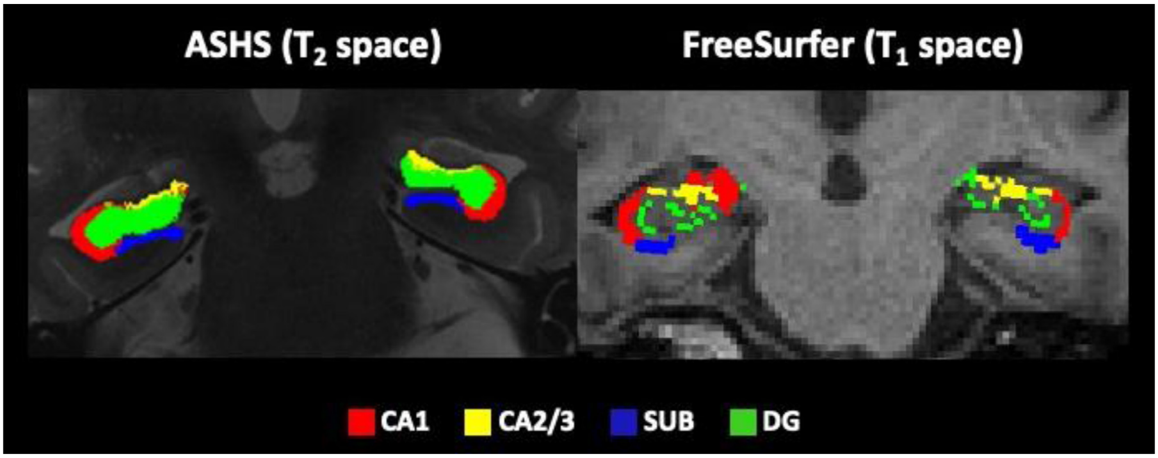

Fig. 1. Displays the hippocampal subfield regions that were automatically segmented from T_1 and T_2-weighted images using the Automated Segmentation of Hippocampal Subfields (ASHS) (Yushkevich et al., 2015b) and the FreeSurfer Segmentation of Hippocampal Subfields functionality (version 6) (Iglesias et al., 2015). Segmentations are shown for 1 participant with coronal images along the anterior-posterior hippocampal axis on a T_2-weighted image for ASHS and a T_1-weighted image for FreeSurfer. Abbreviations: CA1, cornu Ammonis 1; CA2/3; SUB, subiculum; DG, dentate gyrus. "(For interpretation of the references to color in this figure legend, the reader is referred to the Web version of this article.)"

labels, and the extent of specific anatomical labels. The largest discrepancies between the protocols were at the CA1/subiculum boundary and in the anterior portion relative to body and tail portions of the hippocampal formation.

For this reason, we employed the two most widely used automated hippocampal subfield labelling protocols, that is, FreeSurfer version 6.0 and ASHS. We then assessed whether the type of protocol affected the pattern of risk-related differences in macro- and microstructure of the hippocampal formation. We focused our comparison on CA1, CA2/3, DG and subiculum as these regions have previously been implicated in aging and disease and were sufficiently large to extract meaningful microstructural information from diffusion and qMT images with a resolution of approximately 2mm^3 Fig. 1. displays examples of ASHS and FreeSurfer segmentations of these subfields for one representative data set.

While the microstructural measurements described above were chosen to capture complementary tissue properties (Wolf et al., 2015), they also share some overlapping information that can cause redundancies in the data analysis and reduce the statistical power of the analyses (Chamberland et al., 2019). We and others have previously demonstrated that Principal Component Analysis (PCA) can be successfully employed to reduce the dimensionality of multi-modal brain measurements and extract meaningful components of the underlying data structure (Bourbon-Teles et al., 2017; Chamberland et al., 2019; Geeraert et al., 2020; Metzler-Baddeley et al., 2017; Penke et al., 2010).

Here we adopted this approach to study potential dissociations between age- and age-independent risk effects on principal components of hippocampal macro- and microstructure. More specifically, we modelled main and interaction effects of *APOE*, FH, and WHR on three principal components that reflected apparent myelin/neurite packaging, size/complexity, and metabolism of hippocampal gray matter. Differences between hippocampal subfields and between protocols in the pattern of risk effects were modelled by including subfield and protocol as independent factors, which allowed for the testing of interaction effects between risk and these factors. These analyses controlled for the effects of age, sex (Veldsman et al., 2021) and verbal intelligence (Boyle et al., 2021), as we aimed to gain a better understanding of age and sex-independent effects of *APOE*, FH and obesity and their potential interactions. Differences between subfields in the pattern of age and risk effects were further assessed with post-hoc tests.

Finally, we assessed age and risk effects on cognitive functions including episodic memory and spatial navigation and explored brain-function correlations between the hippocampal subfield macro- and microstructure and cognition.

2. Materials and methods

CARDS received ethical approval from the School of Psychology Research Ethics Committee at Cardiff University (EC.14.09.09.3843R2). Participants provided written informed consent in accordance with the Declaration of Helsinki.

2.1. Participants

Participants between the age of 38 and 71 years were recruited from the local community *via* Cardiff University volunteer panels, notice boards and local poster advertisements. A detailed description of the CARDS sample can be found in Mole et al. (2020). All participants had a good command of the English language and were without a history of neurological and/or psychiatric disease, head injury with loss of consciousness, or drug or alcohol dependency. A total of 166 CARDS volunteers underwent MRI scanning at the Cardiff University Brain Research Imaging Centre (CUBRIC). Seven participants did not complete the MRI protocol, including the high resolution T_2 images of the hippocampus, due to claustrophobia and/or feeling uncomfortable. Participants' intellectual function was assessed with the National Adult Reading Test-Revised (NART-R) (Nelson, 1991) and cognitive impairment was screened for with the Mini Mental State Exam (MMSE) (Folstein et al., 1975). One person with a MMSE score of 26 was excluded from the analysis. Thus, the current analysis was based on 158 datasets (see Table 1).

2.2. Assessment of dementia risk factors

Central obesity was assessed with the Waist to Hip Ratio (WHR) following the World Health Organisation's (World Health Organisation, 2008) recommended protocol for measuring waist and hip circumference. Central obesity was defined as a WHR $\geq$0.9 for

Table 1
Summary of demographic, genetic, and lifestyle risk information of participants

n	158
Age (in years)	*M* = 55.7, *SD* = 8.2
Females n	91
NART	*M* = 116.9, *SD* = 6.7
MMSE	*M* = 29.1, *SD* = 0.9
FH+ n	56
APOE ε4+ n	61
Central obesity[a] n	95

Key: *APOE*, Apolipoprotein-E; FH, family history of a dementia; m, mean; MMSE, mini mental state exam (Folstein et al., 1975); NART, national adult reading test (Nelson, 1991); SD, standard deviation.

[a] Based on waist-hip ratio ≥0.9 for males and ≥0.85 for females (Organisation, 2008).

males and ≥0.85 for females. Individuals were categorized as centrally obese (WHR+) or normal WHR (WHR-).

Saliva samples were collected with the Genotek Oragene-DNA kit (OG-500) for DNA extraction and *APOE* genotyping. *APOE* genotypes ε2, ε3, and ε4 were determined by TaqMan genotyping of single nucleotide polymorphism rs7412 and KASP genotyping of single nucleotide polymorphism rs429358. Genotyping was unsuccessful for one individual. Participants were categorized into those who carried at least one ε4 allele (*APOE ε*4) and those who did not (*APOE ε*4-).

Participants also self-reported their family history of dementia, that is, whether a first-grade relative was affected by Alzheimer's disease, vascular dementia or any other type of dementia. Two participants could not provide information about their family history (FH). The remaining participants were categorized into those with a positive FH (FH+) and those without (FH-).

2.3. Cognitive assessment

Immediate and 30 minutes delayed verbal and visual recall were assessed with the Rey Auditory Verbal Learning Test (RAVLT) (Rey, 1941; Schmidt, 1996) and the complex Rey Figure Test (Rey, 1941). Short term topographical memory was measured with the 4 Mountains Test (Chan et al., 2016). Spatial navigation was assessed with a virtual Morris Water Maze Task (Hamilton et al., 2002) where participants had to find and navigate to a hidden platform in a water pool. This task also included a motor control condition without a visible platform. Working memory capacity and executive functions were assessed with computerized tests from the Cambridge Brain Sciences battery (Hampshire et al., 2012; Owen et al., 2010). Working memory capacity was tested with digit and spatial span, distractor suppression with an adapted version of the Stroop test (Double-Trouble), problem solving with a version of the Tower of London task (the Tree task), abstract reasoning with grammatical reasoning and the odd-one-out task, as well as the ability to manipulate and organize spatial information with a self-ordered spatial span task. In addition, participants performed a paired-associate learning (PAL) and a choice-reaction time task. Cognitive outcome measures were the number and latencies of correct responses as well as spatial navigation path length.

2.4. MRI data acquisition

MRI data were acquired on a 3T MAGNETOM Prisma clinical scanner with a 32-channel head coil (Siemens Health Care, Erlangen, Germany). For hippocampal subfield segmentation and volumetric analyses, T_1- and T_2-weighted anatomical images were collected. T_1-weighted images were acquired with a 3-dimension (3D) magnetization-prepared rapid gradient-echo (MP-RAGE) sequence (256 × 256 acquisition matrix, TR = 2300 ms, TE = 3.06 ms, TI = 850ms, flip angle θ = 9°, 176 slices, 1 mm slice thickness, FOV = 256 mm and acquisition time of ~6 minutes). High resolution (0.4 × 0.4 × 2.5 mm voxel) T_2-weighted anatomical images of the hippocampus were acquired with a turbo-spin-echo sequence in the coronal plane with TR = 3300 msec, TE = 84 msec, TI =, flip angle = 155°, 30 slices, 2.5 mm slice thickness, FOV = 256 mm and acquisition time of ~8 minutes.

High Angular Resolution Diffusion Imaging (HARDI) (Tuch et al., 2002) data (2 × 2 × 2 mm voxel) for the NODDI analyses were collected with a spin-echo echo-planar dual shell HARDI sequence with diffusion encoded along 90 isotropically distributed orientations (Jones et al., 1999) (30 directions at b-value = 1200 s/mm^2 and 60 directions at b-value = 2400 s/mm^2) and 6 non-diffusion weighted scans with dynamic field correction and the following parameters: TR = 9400 ms, TE = 67 ms, 80 slices, 2 mm slice thickness, FOV = 256 × 256 × 160 mm, GRAPPA acceleration factor = 2 and acquisition time of ~15 minutes.

Quantitative magnetization transfer weighted imaging (qMT) data were acquired with an optimized 3D MT-weighted gradient-recalled-echo sequence (Cercignani and Alexander, 2006) to obtain magnetization transfer-weighted data with the following parameters: TR = 32 ms, TE = 2.46 ms; Gaussian MT pulses, duration t = 12.8 ms; FA = 5°; FOV = 24 cm, 2.5 × 2.5 × 2.5 mm^3 resolution. The following off-resonance irradiation frequencies (Θ) and their corresponding saturation pulse nominal flip angles (ΔSAT) for the 11 MT-weighted images were optimized using Cramer-Rao lower bound optimization: Θ = [1000 Hz, 1000 Hz, 2750 Hz, 2768 Hz, 2790 Hz, 2890 Hz, 1000 Hz, 1000 Hz, 12060 Hz, 47180 Hz, 56360 Hz] and their corresponding ΔSAT values = [332°, 333°, 628°, 628°, 628°, 628°, 628°, 628°, 628°, 628°, 332°]. The longitudinal relaxation time, T_1, of the system was estimated by acquiring three 3D gradient recalled echo sequence (GRE) volumes with 3 different flip angles (θ = 3°,7°,15°) using the same acquisition parameters as used in the MT-weighted sequence (TR = 32 ms, TE = 2.46 ms, FOV = 24 cm, 2.5 × 2.5 × 2.5 mm^3 resolution). Data for computing the static magnetic field (B_0) were collected using two 3D GRE volumes with different echo-times (TE = 4.92 ms and 7.38 ms respectively; TR= 330 ms; FOV= 240 mm; slice thickness 2.5 mm) (Jezzard and Balaban, 1995).

2.5. Hippocampal subfield segmentations

Whole brain T_1 and high resolution T_2- weighted images were used as input images to segment subregions of the hippocampal formation with the FreeSurfer (version 6.0) (Iglesias et al., 2015) and ASHS (Yushkevich et al., 2015b) hippocampal subfields segmentation tools. Detailed descriptions of the 2 pipelines are available on https://surfer.nmr.mgh.harvard.edu/fswiki/HippocampalSubfields and https://www.nitrc.org/projects/ashs.

In brief, the FreeSurfer version 6.0 cross-sectional segmentation pipeline firstly requires the fully automated analysis of the T_1-weighted images with reconall (http://surfer.nmr.mgh.harvard.edu/) that involves skull stripping, correction for motion artefacts and field inhomogeneities, the registration of native data to and from the standard Talairach space, parcellation of cortical regions and the segmentation of subcortical structures as well as the hippocampi (Fischl, 2012). These processing steps were followed by a hippocampal subfield segmentation pipeline that utilises both T_1 and T_2- weighted images to identify anatomical landmarks for the bilateral segmentation of 12 subfields, that is, CA1, CA2/3, CA4, subiculum, presubiculum, parasubiculum, molecular layer of the subiculum and CA fields, granule cell layer of the dentate gyrus, fimbria, hippocampus-amygdala transition area, hippocampal tail, and fissure (Iglesias et al., 2015). This pipeline is based on a statistical atlas of the hippocampus constructed from manual segmentation labels from both *in vivo* and high-resolution *ex vivo* data that were used to develop a Bayesian inference algorithm for the automatic segmentation of the hippocampus proper from T_1 and T_2-weighted structural images (Iglesias et al., 2015).

The ASHS software (https://sites.google.com/site/hipposubfields) implements a multi-atlas segmentation technique that involves registering the target MRI with a bank of T_2-weighted atlas MRIs including manually labeled subregions. Here the ASHS UPenn PMC Atlas package was chosen for this purpose. Multi-atlas label fusion is then applied to select a consensus segmentation based on the shared similarity between target and atlas images. Systematic segmentation errors are minimized with a learning-based bias correction technique. Joint label fusion and corrective learning are then repeated by bootstrapping seeded by the segmentation results from the previous phase. ASHS leads to the segmentation of 10 region of interests, that is, CA1, CA2, CA3, DG, subiculum, entorhinal cortex, Brodmann area 35, Brodmann area 36, collateral sulcus and miscellaneous regions. To allow meaningful extraction of lower resolution microstructural data, ASHS CA2 and CA3 regions were combined using the fslmaths utility from the Oxford Centre for Functional MRI of the Brain (FMRIB) Software Library (version 6.0) (Jenkinson et al., 2012) .

For the purpose of comparing between the two segmentation techniques and for allowing meaningful extraction of lower resolution microstructural values, the present analysis focused on CA1, CA2/3, DG and subiculum regions that were shown to be affected by aging and AD (de Flores et al., 2015a). For quality control, FreeSurfer and ASHS labels of these regions were visually inspected by authors BC and PAG.

Mean hippocampal subfield and intracranial volumes (ICV) were extracted for each brain. Subfield volumes were then adjusted for ICV to correct for inter-individual differences in head size using the formula (subfield volume x 1000)/ ICV (from FreeSurfer or ASHS respectively).

2.6. HARDI and qMT data processing

A detailed description of the microstructural data processing has been provided previously (Metzler-Baddeley et al., 2019a; Metzler-Baddeley et al., 2019b). In brief, the dual-shell HARDI data were split and b = 1200 and 2400 s/mm^2 data were corrected separately for distortions induced by the diffusion-weighted gradients and motion artifacts with appropriate reorientation of the encoding vectors (Leemans and Jones, 2009) in ExploreDTI (Version 4.8.3) (Leemans et al., 2009). EPI-induced geometrical distortions were corrected by warping the diffusion-weighted image volumes to the T_1 –weighted anatomical images (Irfanoglu et al., 2012). After preprocessing, the NODDI model (Zhang et al., 2012) was fitted to the HARDI data with the fast, linear model fitting algorithms of the Accelerated Microstructure Imaging via Convex Optimization (AMICO) framework (Daducci et al., 2015) to gain ISOSF, ICSF, and ODI maps.

Using Elastix (Klein et al., 2010), MT-weighted GRE volumes were co-registered to the MT-volume with the most contrast using a rigid body (6 degrees of freedom) registration to correct for inter-scan motion. Data from the 11 MT-weighted GRE images and T_1-maps were fitted by a two-pool model using the Ramani pulsed-MT approximation (Ramani et al., 2002). This approximation provided MPF, k_f and R_1 maps. MPF maps were thresholded to an upper intensity limit of 0.3 and k_f maps to an upper limit of 3.0 using the FMRIB's fslmaths imaging calculator to remove voxels with noise-only data.

All microstructural maps were spatially aligned with the hippocampal subfield masks by co-registration with the T_1- weighted anatomical space as reference image with linear affine registration (12 degrees of freedom) using FMRIB's Linear Image Registration Tool. Spatial alignment of microstructural maps to ASHS hippocampal subfield masks involved an additional warping to the T_2-weighted space with FMRIB's Linear Image Registration Tool.

2.7. Statistical analysis

Statistical analyses were conducted in SPSS version 26 (IBM, 2011). All volumetric, microstructural, and cognitive data were examined for normal distribution and for outliers, defined as above or below 3 times the interquartile range (75th percentile value - 25th percentile value).

2.7.1. Missing data

FreeSurfer hippocampal subfield segmentations could be performed for all 158 datasets and ASHS segmentations for a total of 153 datasets. For FreeSurfer one volume and for ASHS two volume measurements were excluded as outliers. For the microstructural data, 1% of the data were excluded as outliers for FreeSurfer and 5% for ASHS segmentations. For the cognitive data 2.3% of the data were either missing or excluded as outliers.

For the principal component analysis (PCA), each participant's volumetric and microstructural data of the 16 hippocampal subfield segmentations [2 (FreeSurfer, ASHS) x 2 (left, right) x 4 (CA1, CA2/3, DG, subiculum)] were concatenated to form n = 2528 observations. The dependent variables were represented by the 7 brain measurements (ICV-adjusted volumes, MPF, k_f, R_1, ODI, ISOSF, ICSF). Bartlett's test of sphericity and the Kaiser-Meyer-Olkin (KMO) test were used to check that the data were suitable for PCA [KMO = 0.57, Chi^2 (21) = 2842.2, $p < 0.001$]. PCA was then carried out using a procedure with orthogonal Varimax rotation of the component matrix. Components were extracted based on the Kaiser criterion of including all components with an eigenvalue >1 (IBM, 2011), by inspecting Cattell's scree plots (Cattell, 1952), and by assessing each component with regards to their interpretability. Component loadings that exceeded a value of 0.5 were considered as significant. The dimensionality of the cognitive data for all 158 participants was also reduced with PCA using the same procedure as described above [KMO = 0.61, Chi^2 (630) = 2463.37, $p < 0.001$].

Each participant's PCA least squares regression component scores (DiStefano et al., 2009) were subsequently entered as dependent variables in a multivariate analysis of covariance (MANCOVA) that tested for main and interaction effects of the risk factors *APOE* genotype (ε4+, ε4-), FH (FH+, FH-), and WHR (WHR+, WHR-) as well as for the effects of the segmentation protocol (FreeSurfer, ASHS) and hippocampal subfield segmentations (bilateral CA1, CA2/3, DG, subiculum). Age, sex and IQ-scores from the NART-R (Nelson, 1991) were included as covariates. Similarly, MANCOVA tests for risk effects on cognitive component scores, while controlling for age, sex, and IQ, were completed.

Significant omnibus effects were further investigated with post-hoc comparisons using univariate analysis of covariance (ANCOVA) and independent t-tests. Relationships between brain structure and cognitive component scores were studied using hierarchical linear regression models that first entered age and sex as independent variables, and then in a second model volumetric and microstructural measurements **o**f all left and right CA1, CA2/3, DG, and subiculum regions segmented with ASHS and FreeSurfer in a stepwise fashion to predict the variance in the cognitive component data.

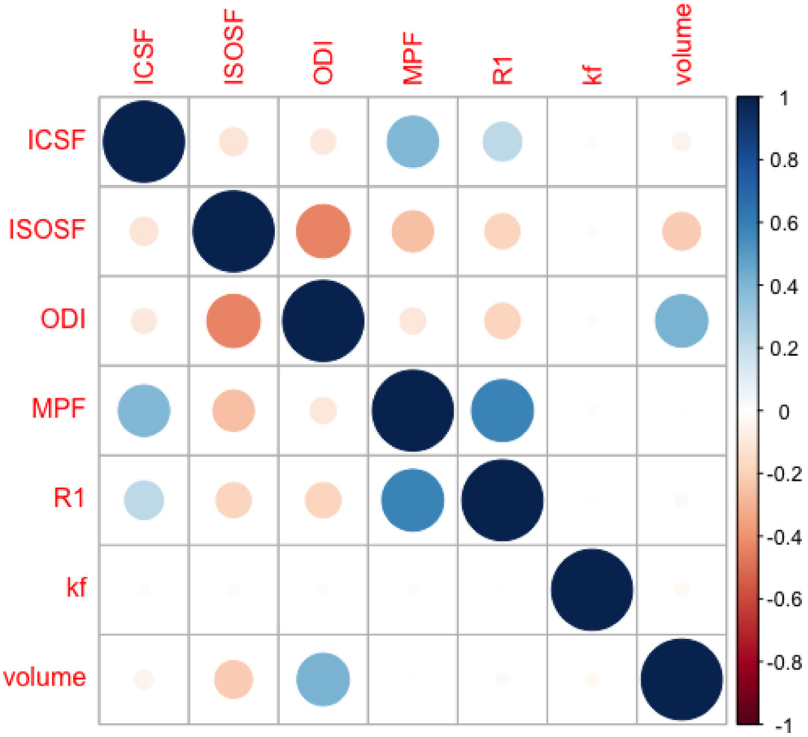

Fig. 2. Correlation matrix of the microstructural variables that were entered into the Principal Component Analysis. Positive correlations are displayed in blue and negative correlations in red. Abbreviations: ICSF, intracellular signal fraction; ISOSF, isotropic signal fraction; k_f, forward exchange rate; MPF, macromolecular proton fraction; ODI, orientation dispersion index; R_1, longitudinal relaxation rate; volume, volume adjusted for intracranial volume. "(For interpretation of the references to color in this figure legend, the reader is referred to the Web version of this article.)"

First and post-hoc models were corrected for multiple comparisons with a False Discovery Rate (FDR) of 5% using the Benjamini-Hochberg procedure (Benjamini and Hochberg, 1995). The 5% FDR was applied to all statistical tests that related to the same theoretical inference (Lakens, 2014).

All reported *p*-values, unless stated otherwise, were Benjamini-Hochberg adjusted (p_{BHadj}) and two-tailed. Information about effects sizes was provided with the partial eta squared index $\eta_p{}^2$ for MANCOVA analyses and R^2 for regression analyses.

3. Results

3.1. Principal Component Analysis (PCA) of brain measurements

Fig. 2 displays the correlation matrix of the microstructural variables that were entered into the PCA. The variables MPF, R_1 and ICSF were positively correlated with each other, as were ODI and volume. ISOSF was negatively correlated with ODI, MPF, R_1, ICSF and volume. There were no correlations with other measures for k_f.

Consistent with this cross-correlation pattern, PCA extracted three components that explained 67% of the variance in the hippocampal macro- and microstructural data (Table 2). The first component explained 28.2% of the data variance and had positive loadings >0.5 from MPF, R_1 and ICSF sensitive to myelin and neurite packing. The second component explained an additional 24.5% of the variance and had positive loadings > 0.5 from ODI and ICV-adjusted volumes and a negative loading from ISOSF and thus captured tissue size and complexity. The third component explained 14.3% of variance and had a high loading from k_f only and may reflect tissue metabolism.

3.2. Multivariate analysis of covariance (MANCOVA) of macro- and microstructural PCs

3.2.1. Omnibus effects

There were significant main effects for age [F(3,2124) = 13.72, $p_{BHadj} < 0.001$, $\eta_p{}^2 = 0.02$], sex [F(3,2124) = 22.24, $p_{BHadj} < 0.001$, $\eta_p{}^2 = 0.03$], WHR [F(3,2124) = 6.8, $p_{BHadj} < 0.001$, $\eta_p{}^2 = 0.01$], protocol [F(3,2124) = 128.7, $p_{BHadj} < 0.001$, $\eta_p{}^2 = 0.15$] and hippocampal subfield [F(9,6378) = 322.2, $p_{BHadj} < 0.001$, $\eta_p{}^2 = 0.3$]. Significant interaction effects were present between protocol and hippocampal subfield [F(9,6378) = 111.29, $p_{BHadj} < 0.001$, $\eta_p{}^2 = 0.14$] and between *APOE* and WHR [F(3,2124) = 5.51, $p_{BHadj} = 0.005$, $\eta_p{}^2 = 0.008$].

3.2.2. Post hoc effects

Protocol and hippocampal subfield had significant effects on the myelin/neurite packing PC1 [Protocol: F(1,2126) = 21.5, $p_{BHadj} < 0.001$, $\eta_p{}^2 = 0.01$; Subfield: F(3,2126) = 236.7, $p_{BHadj} < 0.001$, $\eta_p{}^2 = 0.25$] and the size/complexity PC2 [Protocol: F(1,2126) = 381.7, $p_{BHadj} < 0.001$, $\eta_p{}^2 = 0.15$; Subfield: F(3,2126) = 1483.2, $p_{BHadj} < 0.001$, $\eta_p{}^2 = 0.68$]. Overall ASHS relative to FreeSurfer segmentations had smaller PC1 values [t(2248) = -3.9, $p_{BHadj} < 0.001$] (Fig. 3A) but larger PC2 values [t(2248) = 11.2, $p_{BHadj} < 0.001$] (Fig. 3B). With regards to the subfields, subiculum was associated with the largest PC1 myelin/neurite packing values (Fig. 3C), while CA2/3 had the lowest PC2 size/complexity values (Fig. 3D). No effects were observed for the PC3 Metabolite component.

Furthermore, protocol and subfields interacted with each other in both components [PC1: F(3,2126) = 37.1, $p_{BHadj} < 0.001$, $\eta_p{}^2 = 0.05$; PC2: F(3,2126) = 385.7, $p_{BHadj} < 0.001$, $\eta_p{}^2 = 0.35$] (Fig. 4). FreeSurfer compared with ASHS segmentations were

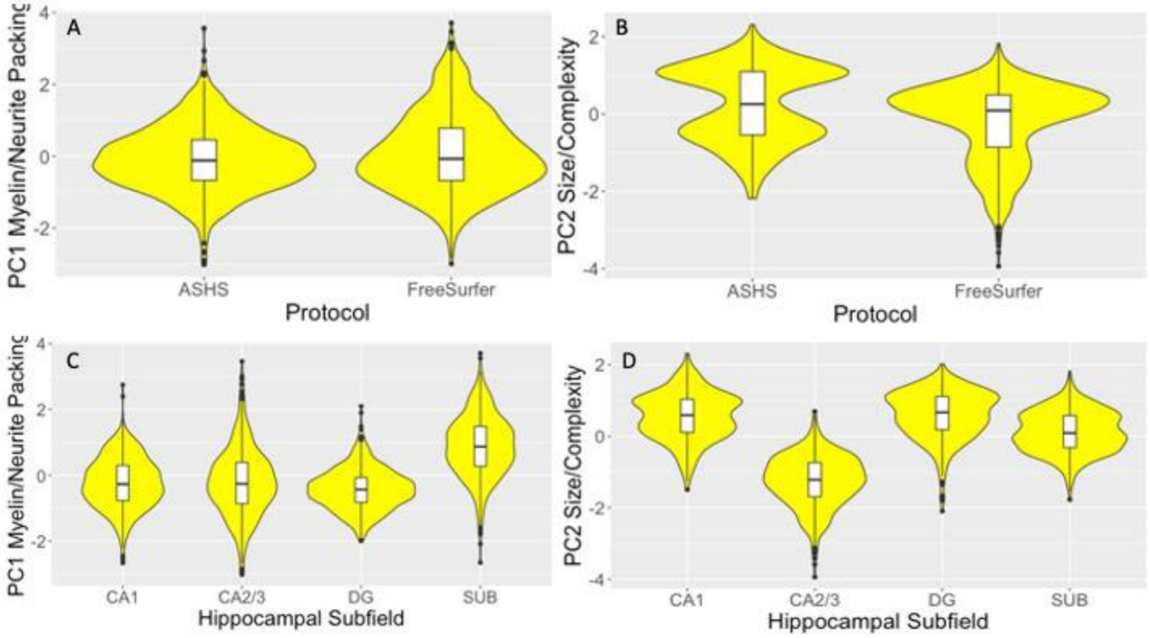

Fig. 3. Violin plots with overlaid box plots of the difference between; A) the Automatic Segmentation of Hippocampal Subfields (ASHS) and the FreeSurfer (version 6) segmentation protocols in the myelin/neurite packing principal component (PC); B) in the size/complexity PC, C) between the hippocampal subfields cornu Ammonis (CA) 1, CA2/3, dentate gyrus (DG) and subiculum in the myelin/neurite packing PC; D) in the size/complexity PC. Boxplots display the median and the interquartile range and violin plots the kernel probability density, that is, the width of the yellow area represents the proportion of the data located there. "(For interpretation of the references to color in this figure legend, the reader is referred to the Web version of this article.)"

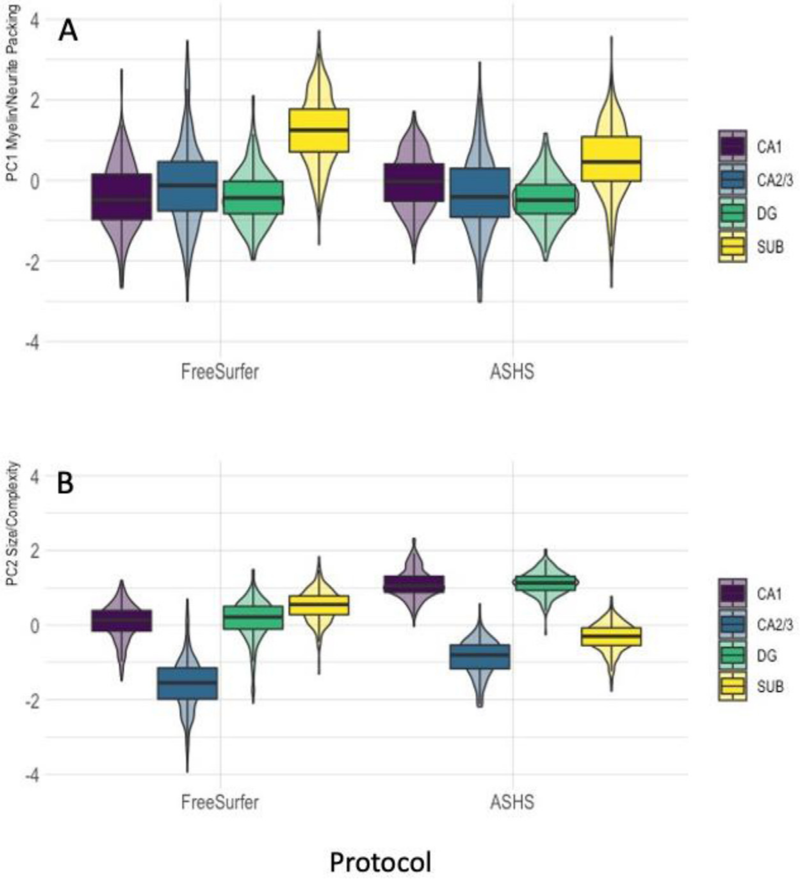

Fig. 4. Violin plots with overlaid box plots displaying the effects of protocol as a function of hippocampal subfields on (A) the myelin/neurite packing principal component; (B) the size/complexity component. Boxplots display the median and the interquartile range and violin plots the kernel probability density. Abbreviations: ASHS, automated segmentation of hippocampal subfields; CA, cornu Ammonis; DG, dentate gyrus; SUB, subiculum. "(For interpretation of the references to color in this figure legend, the reader is referred to the Web version of this article.)"

Table 2

Rotated component matrix of the principal component analysis within the macro- and microstructural data from FreeSurfer and ASHS hippocampal subfields (N = 2528)[a]

	PC1 Myelin/neurite packing	PC2 Size/Complexity	PC3 Metabolism
ICSF *Neurite density*	**0.62**	-0.05	-0.02
ISOSF *Free Water*	-0.34	**-0.71**	-0.10
ODI *Neurite dispersion*	-0.21	**0.85**	0.01
MPF *apparent myelin*	**0.88**	0.05	0.003
R_1 *apparent myelin, iron*	**0.80**	-0.02	0.005
k_f *metabolism*	-0.02	-0.02	**0.99**
ICV-adjusted volume	-0.05	**0.70**	-0.08

Key: ICSF, intracellular signal fraction; ICV, intracranial volume; ISOSF, isotropic signal fraction; k_f, forward exchange rate; MPF, macromolecular proton fraction; ODI, orientation dispersion index; R_1, longitudinal relaxation rate.

[a] Rotation Method: Varimax with Kaiser normalization.

associated with larger PC1 myelin/neurite packing values, primarily due to larger values in the subiculum (Fig. 4A). In contrast, ASHS compared with FreeSurfer segmentations showed larger PC2 size/complexity values (Fig. 4B), due to larger estimations in CA1, CA2/3 and DG but not subiculum.

Age had a significant effect on the myelin/neurite packing PC1 [F(1,2126) = 37.3, $p_{BHadj} < 0.001$, $\eta_p^2 = 0.02$]. More specifically, age was associated with a reversed U-shape in PC1 values having a peak in the forties, with youngest and oldest participants showing the lowest values (Fig. 5A). Sex had an effect on the size/complexity PC2 [F(1,2126) = 56.3, $p_{BHadj} < 0.001$, $\eta_p^2 = 0.03$], with males showing reduced PC2 values compared with females [t(2279) = 5.3, $p_{BHadj} < 0.001$] (Fig. 5B).

WHR affected myelin/neurite packing and size/complexity components [PC1: F(1,2126) = 11.6, $p_{BHadj} = 0.002$, $\eta_p^2 = 0.005$; PC2: F(1,2126) = 5.5, $p_{BHadj} = 0.036$, $\eta_p^2 = 0.003$] as centrally obese individuals relative to those with a normal WHR had lower values in both components [PC1: t(2231) = 4.14, $p_{BHadj} < 0.001$; PC2: t(2231) = 4.15, $p_{BHadj} < 0.001$] (Fig. 6). Moreover, WHR interacted with *APOE* on size/complexity [F(1,2126) = 15.2, $p_{BHadj} < 0.001$, $\eta_p^2 = 0.007$] (Fig. 7). While *APOE* ε4- individuals with a normal WHR had a larger size/complexity component than overweight/obese *APOE* ε4- individuals [t(1341) = 4.14, $p_{BHadj} < 0.001$], this was not the case for *APOE* ε4+ individuals [t(880) = 1.6, p= 0.1] (Fig. 7).

3.3. Exploring the pattern of age and risk effects across hippocampal subfields

To explore the patterns of age and risk effects across the 4 hippocampal subfields CA1, CA2/3, DG, and subiculum, separate ANCOVAs were carried out on the PC data for each subfield concatenated across hemisphere and protocol.

Significant age effects (controlled for sex and NART-R IQ) on the myelin/neurite packing PC1 were observed for CA1 [F(4,564) = 12.9, $p_{BHadj} < 0.001$, $\eta_p^2 = 0.08$], for CA2/3 [F(4,567) = 5.7, $p_{BHadj} < 0.001$, $\eta_p^2 = 0.04$], for DG [F(4,556) = 7.4, $p_{BHadj} < 0.001$, $\eta_p^2 = 0.05$] and subiculum [F(4,568) = 11.7, $p_{BHadj} < 0.001$, $\eta_p^2 = 0.08$].

Trends for WHR effects (controlled for age, sex and NART-R IQ) on the size/complexity PC2 were present in CA1 ($p_{BHadj} = 0.06$), CA2/3 ($p_{BHadj} = 0.06$) and DG ($p_{BHadj} = 0.09$) but not for the subiculum ($p = 0.6$). Trends for interaction effects between *APOE* and WHR were present for CA1 ($p = 0.06$) and DG ($p = 0.06$) but not for CA2/3 ($p = 0.32$) or subiculum ($p = 0.6$).

3.4. PCA of the cognitive data

Four principal components were extracted that explained together 44% of the variance in the cognitive data (Table 3). The first PC labelled “Verbal Memory” explained 15.2% of the variance and had high loadings >0.5 from RAVLT measures. The second PC “Spatial Navigation First Move” explained 13.5% of the variance with loadings from first move latencies in the virtual spatial navigation task. The third PC “Spatial Navigation Path Length” explained an additional 9.5% of the variance with loadings from spatial navigation path length. The fourth PC “Visual Memory” explained 5.8% of data variance and had loadings from immediate and delayed recall of the Rey figure and from the 4 Mountains Test.

3.5. MANCOVA of cognitive PCs

There were significant omnibus effects of age [F(4,99) = 7.2, $p_{BHadj} < 0.001$, $\eta_p^2 = 0.23$] and sex [F(4,99) = 22.24, $p_{BHadj} =0.02$, $\eta_p^2 = 0.14$]. Age affected first move latencies in the spatial navigation task [F(1,102) = 19.6, $p_{BHadj} < 0.001$, $\eta_p^2 = 0.16$] such that latencies increased with age (r = 0.38, $p < 0.001$). Sex had an effect on verbal recall performance [F(1,102) = 10.6, $p_{BHadj} = 0.008$, $\eta_p^2 = 0.16$] with women performing better in the RAVLT than men. There were no effects of risk.

3.6. Regression analysis of brain-cognition relationships

Table 4 summarizes the results of the linear hierarchical regression analyses. As age and sex had significant effects on the cognitive components, they were first entered as independent variables prior to testing for the effects of hippocampal subfield macro- and microstructure in a stepwise fashion. A final model that included contributions from left CA1 ODI and right DG ISOSF explained 14% of the Verbal Recall data, while 24% of the Visual Recall data were explained by right CA2/3 ICSF and right CA1 volume and ISOSF. For spatial navigation first move latencies, 31% of the data were explained by a model including age, sex, and left CA2/3 R_1, while for path length 19% of the data were explained by right subiculum ODI and left subiculum ISOSF and k_f.

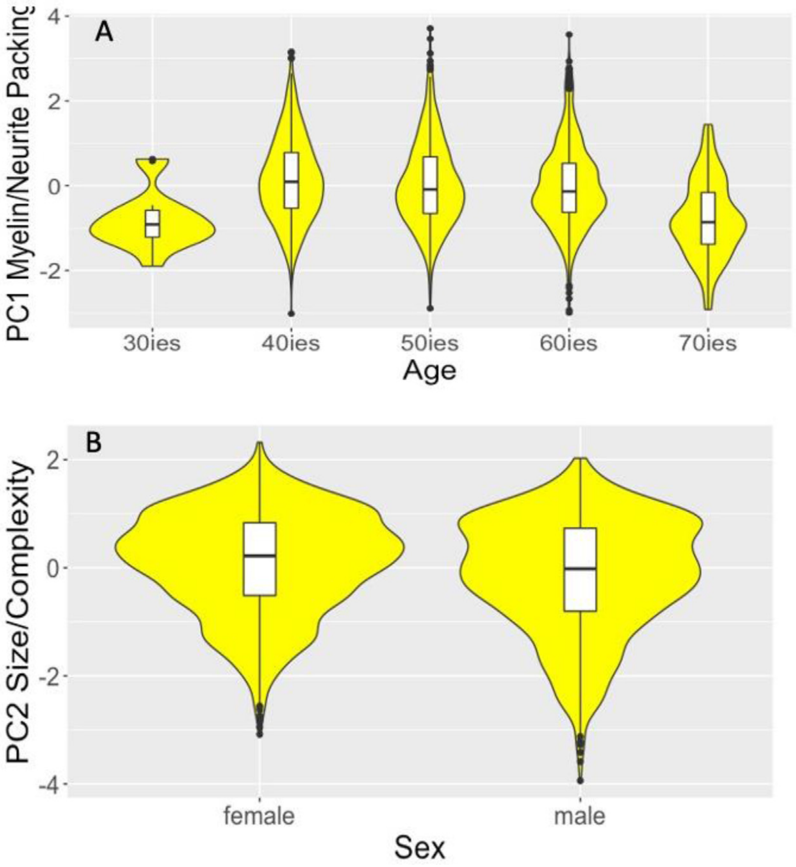

Fig. 5. Violin plots with overlaid box plots displaying the effects of (A) age on the myelin/neurite packing principal component (PC) and (B) of sex on the size/complexity PC. Boxplots display the median and the interquartile range and violin plots the kernel probability density. "(For interpretation of the references to color in this figure legend, the reader is referred to the Web version of this article.)"

4. Discussion

Dissociating the effects of healthy aging on hippocampal subfields from those related to genetic and lifestyle risk of dementia could be key to effectively targeting interventions for older-age memory impairments. Thus, the primary objective of the present study was to investigate age and age-independent effects of three major risk factors, that is, carriage of the *APOE* $\varepsilon 4$ genotype, a positive family history (FH) of dementia, and central obesity, on the macro- and microstructure of the hippocampal formation in a sample of 158 cognitively healthy adults.

We characterized properties of the hippocampal formation with subfield volumes based on T_1 and high-resolution T_2-weighted images as well as with microstructural measurements from NODDI and qMT imaging to gain complementary information about apparent myelin, neurite packing, free water, and metabolism. Accounting for overlapping information between the various MRI measurements, PCA was employed to reduce the data dimensionality to three principal components that reflected myelin/neurite packing, size/complexity, and metabolic tissue properties. These components were then investigated across the main subfields of the hippocampal formation, that is, CA1, CA2/3, DG, and subiculum, which were previously shown to be particularly vulnerable to the impact of aging and disease (de Flores et al., 2015b). Subfields were segmented using two widely employed and freely available, automated segmentation protocols, that is, ASHS and FreeSurfer (version 6). This allowed us to assess any potential interaction effects between the type of protocol and risk factors on the analysis of hippocampal subfield properties.

While type of labelling protocol and hippocampal subfields were associated with absolute differences in component measures, they did not interact with the risk factors, suggesting that risk effects did not significantly differ between ASHS and FreeSurfer segmentations. Overall ASHS relative to FreeSurfer segmentations resulted in larger size/complexity but lower myelin/neurite packing estimates (Fig. 3). ASHS segmentations of CA1, CA2/3 and DG were larger, but subiculum labels were smaller than those of FreeSurfer (Fig. 4).

These differences were caused by disagreements in the anatomical labels between the two segmentation protocols that are known to be most pronounced at the CA1/subiculum boundary and within the anterior portion of the hippocampal formation (Yushkevich et al., 2015a). In addition, both protocols differed in the region of the hippocampal formation that was labelled and the number of subfield segmentations. While FreeSurfer labels 12 regions (CA1, CA2/3, CA4, subiculum, presubiculum, parasubiculum, molecular layer of the subiculum and CA fields, granule cell layer of the dentate gyrus, fimbria, hippocampus-amygdala transition area, hippocampal tail, and fissure) (Iglesias et al., 2015), ASHS segments ten structures (CA1, CA2, CA3, DG, subiculum, entorhinal cortex, Brodmann area 35, Brodmann area 36, collateral sulcus and miscellaneous regions) (Yushkevich et al., 2015b). As many of these subfields were too small to extract meaningful lower resolution microstructural information, we focused on the analysis of the 4 main subfields of the hippocampal formation that were labelled by both protocols (CA1, CA2/3, DG and subiculum).

However, these subfield labels did not correspond to exactly the same regions across the two protocols. Notably, FreeSurfer

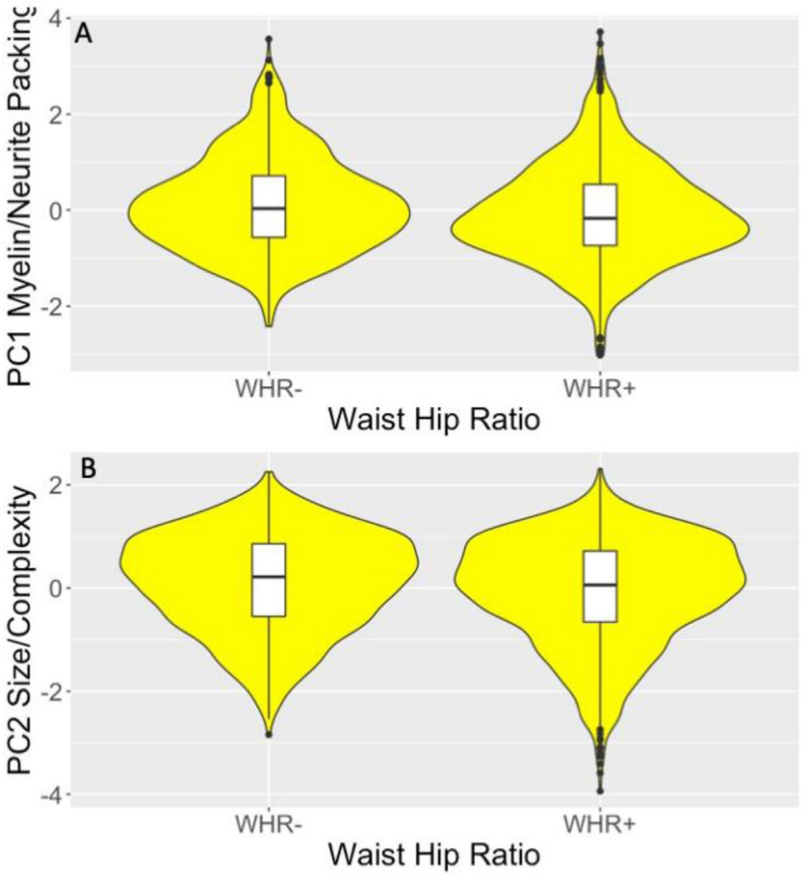

Fig. 6. Violin plots with overlaid box plots displaying the effects of Waist-Hip-Ratio (WHR) on (A) the myelin/neurite packing principal component (PC); (B) the size/complexity PC. Boxplots display the median and the interquartile range and violin plots the kernel probability density. "(For interpretation of the references to color in this figure legend, the reader is referred to the Web version of this article.)"

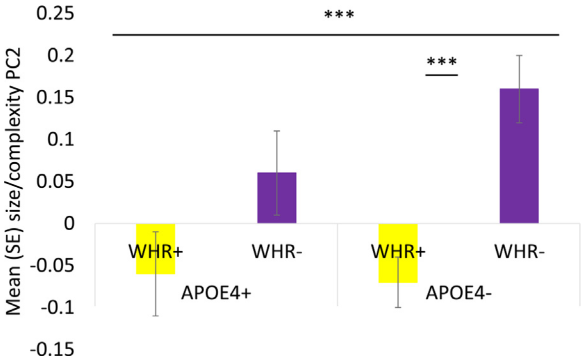

Fig. 7. Column figure displaying the mean and standard errors of the size/complexity principal component (PC) as a function of Apolipoprotein E (*APOE*) genotype and Waist-Hip-Ratio (WHR). Abbreviations: APOE4+, *APOE* ε4 carriers; APOE4-, *APOE* ε4 non-carriers; WHR+, individuals with WHR in abdominal overweight/obese range; WHR-, individuals with WHR in healthy range. *** $p_{BHadj} < 0.001$. "(For interpretation of the references to color in this figure legend, the reader is referred to the Web version of this article.)"

provides a separate label for the "molecular layer" and voxels classified as such were missing from its CA field segmentations while they were part of the ASHS labels. Similarly, the DG label from FreeSurfer only contains the unmyelinated granule cell layer while ASHS labels the whole DG structure including molecular, granule, and inner polymorphic layers. These differences are evident in the example of the ASHS and FreeSurfer segmentations for one dataset displayed in Fig. 1. Together with disagreements about the CA1/subiculum border, they account for the observed size/complexity differences between the two protocols.

However, there were also similarities between the protocols, that were consistent with the known cellular composition and microstructural properties of different hippocampal subfields (Benes et al., 1994; Geurts et al., 2007; Seress et al., 1993; Seress et al., 1992; Seress et al., 1994). Notably, myelin/neurite packing signals were largest in the subiculum for both ASHS and FreeSurfer (Fig. 4). This is consistent with evidence from histological studies using myelin-staining of a higher proportion of myelinated axons in the subiculum compared to other hippocampal regions such as CA1 or the molecular and granule cell layers of the DG (Benes et al., 1994; Geurts et al., 2007; Seress et al., 1994). In addition, both ASHS and FreeSurfer labelled CA2/3 as the smallest structure, while CA1 and DG were comparable in size/complexity consistent with the known anatomy of the hippocampus.

It should also be noted that the final ASHS segmentation outputs were in high resolution T_2-weighted space while those for FreeSurfer were in T_1-weighted space (Fig. 1) suggesting differences in the use of multi-spectral information between the pipelines. A recent study found significant variations in FreeSurfer volume estimations of hippocampal subfields depending on the input images (T_1 and/or T_2) (Seiger et al., 2021). It is therefore possible that differences in the use of standard T_1 and high-resolution T_2-based information may have contributed to the discrepancies observed between the two protocols. Importantly though for our primary research question, despite these significant differences between the ASHS and FreeSurfer labels, there were no interaction

Table 3
Rotated component matrix of the principal component analysis of the cognitive performance[a]

Cognitive tests	Components			
	Verbal memory	Spatial navigation first moves	Spatial navigation path length	Visual memory
RAVLT list A 1st IR	**0.78**	0.01	-0.02	0.06
RAVLT list A 2nd IR	**0.85**	0.02	-0.03	0.01
RAVLT list A 3rd IR	**0.84**	0.09	-0.01	-0.03
RAVLT list A 4th IR	**0.81**	0.02	-0.05	-0.17
RAVLT list A 5th IR	**0.75**	0.03	-0.01	-0.08
RAVLT list B 1st IR	0.47	-0.25	-0.06	0.06
RAVLT list A 6th RaD	**0.81**	-0.02	0.07	0.13
RAVLT list A DR	**0.81**	0.01	0.02	0.14
4 mountains test	0.23	-0.10	-0.23	**0.50**
Rey copy	0.13	-0.13	0.06	0.43
Rey figure IR	-0.02	-0.09	-0.02	**0.80**
Rey figure DR	0.02	-0.03	-0.04	**0.85**
Digit span	0.13	-0.27	-0.09	0.001
Spatial span	-0.14	-0.06	-0.23	0.30
Double trouble	-0.01	-0.16	-0.21	0.19
Tree task	0.07	-0.04	-0.09	-0.21
Odd 1 out	-0.07	-0.16	-0.02	-0.03
Paired associate learning	0.09	-0.11	-0.25	-0.20
Self-ordered search	-0.28	0.02	–0.11	-0.07
Grammatical reasoning	0.01	-0.29	-0.02	0.06
Choice reaction time	-0.01	0.41	0.15	-0.34
Spatial navigation:				
FM block 2	0.35	**0.75**	-0.07	-0.03
FM block 3	0.01	**0.78**	-0.15	0.03
FM block 4	-0.05	**0.76**	-0.22	-0.02
FM block 5	0.01	**0.67**	-0.40	0.01
FM block 6	-0.2	**0.74**	0.03	-0.03
TL block 2	-0.04	**0.63**	0.44	-0.06
TL block 3	0.18	0.35	0.32	-0.22
TL block 4	0.12	0.41	0.45	-0.25
TL block 5	-0.23	0.43	**0.57**	-0.16
TL block 6	-0.11	**0.66**	0.09	-0.30
PL block 2	-0.02	-0.001	**0.68**	0.08
PL block 3	0.22	-0.22	**0.58**	-0.02
PL block 4	0.15	-0.14	**0.71**	-0.09
PL block 5	-0.16	-0.08	**0.80**	-0.03
PL block 6	-0.16	-0.06	0.09	-0.45

Loadings >0.5 are highlighted in bold.
Key: DR, delayed recall; IR, immediate recall; RaD, recall after distraction; RAVLT, Rey auditory verbal learning test.
[a] Rotation method: Varimax with Kaiser normalization.

Table 4
Results of hierarchical stepwise regression analyses testing first for the effects of age and sex and secondly for the effects of macro- and microstructural measurements from CA1, CA2/3, dentate gyrus and subiculum on cognitive components

Cognitive component	R^2	*F*-value (p_{BHadj})	Final Model predictors (β, t-value, p_{BHadj})
PC1 verbal recall	**0.14**	**3.0 (0.02)**	**left CA1$_{FS}$ ODI (-0.3, -2.6, 0.03)** **right DG$_{FS}$ ISOSF (-0.3, -2.3, 0.04)**
PC2 spatial navigation FML	**0.31**	**6.7 (0.002)**	**Age (0.4, 3.5, 0.01)** **Sex (0.3, 2.9, 0.02)** **left CA2/3$_{FS}$ R$_1$ (0.3, 2.8, 0.02)**
PC3 spatial navigation PL	**0.19**	**3.4 (0.01)**	**right SUB$_{FS}$ ODI (0.4, 3.6, 0.01)** **left SUB$_{ASHS}$ ISOSF (-0.3, -2.5, 0.04)** **left SUB$_{FS}$ k_f (-0.3, -2.2, 0.04)**
PC4 visual recall	**0.24**	**4.6 (0.002)**	**right CA2/3$_{ASHS}$ ICSF (-0.3, -3.2, 0.01)** **right CA1$_{FS}$ ISOSF (-0.4, -3.0, 0.02)** **right CA1$_{ASHS}$ volume (-0.3, -2.5, 0.04)**

Key: ASHS, automated segmentation of hippocampal subfields; CA, cornu ammonis; DG, dentate gyrus; FML, first move latency; FS, FreeSurfer; PC, principal component; PL, path length; p_{BHadj}, Benjamini-Hochberg adjusted p-value significant at 5% false discovery rate; SUB, subiculum.

effects between the type of protocol and any of the three risk factors, suggesting that a comparable risk pattern was observed across both protocols.

With regards to risk factors, we observed that central obesity as measured with the WHR was associated with reductions in the myelin/neurite packing and the size/complexity but not the metabolic component (Fig. 6). These findings are consistent with accumulating evidence that obesity is associated with adverse effects on the hippocampus and memory functions (Anan et al., 2010; Dekkers et al., 2019; Khan, et al., 2015; Mueller et al., 2012; Spencer et al., 2017; Stranahan, 2015; Willette and Kapogiannis, 2015). For instance, a recent analysis of data from 12,000 participants (45-76 years of age) of the UK Biobank study, reported that total body fat was related to smaller volumes in subcortical structures and the hippocampi in men (Dekkers et al., 2019). This study also reported obesity-related differences in whole brain white matter microstructure measured with fractional anisotropy and mean diffusivity. Similarly, previous analyses of CARDS data found WHR to be positively correlated with hippocampal atrophy [as estimated with the free water signal (ISOSF)] and negatively with fornix MPF and k_f (Metzler-Baddeley et al., 2019a). In this study, WHR was an estimate of abdominal visceral ($r = 0.3$, $p = 0.001$) but not subcutaneous fat fractions ($p = 0.7$) while Body Mass Index estimated subcutaneous ($r = 0.4$, $p < 0.001$) but not visceral fat ($p = 0.3$) (Metzler-Baddeley et al., 2019a). As Body Mass Index had no effects on brain microstructure, these findings suggest that the correlations between WHR and hippocampal and fornix microstructure were driven by excessive visceral rather than body fat *per se*, consistent with accumulating evidence for visceral fat-related adverse effects on the hippocampus, brain white matter, and mortality (Anan et al., 2010; Koster et al., 2015; Koster and Schaap, 2015; Koster et al., 2010; Lampe et al., 2019). Comparable to Dekkers et al. (2019), men were more centrally obese and had higher visceral fat fractions and higher hippocampal ISOSF (Metzler-Baddeley et al., 2019a).

Central obesity, notably excessive visceral fat, is associated with multiple metabolic alterations affecting blood cholesterol, glucose, and insulin levels, that can lead to cardio- and cerebrovascular disease and Type 2 diabetes (Dommermuth and Ewing, 2018; Whitmer et al., 2007). Central obesity at midlife may also be accompanied with systemic, low-grade inflammation (Cox et al., 2015; Guillemot-Legris and Muccioli, 2017). Diet-induced obesity in animal studies has been shown to trigger inflammation in the hippocampus, which in turn impaired synaptic functioning and spatial memory (Hao et al., 2016). In humans, individuals with a genetic polymorphism associated with pro-inflammatory state and AD risk had smaller CA1-2, CA3-DG and subiculum than healthy controls (Raz et al., 2015). All of those obesity-related metabolic changes in lipid, glucose and immune responses are thought to contribute to the risk of developing dementia in older age (Businaro et al., 2018; Profenno et al., 2010; Ricci et al., 2017).

Furthermore, it is also increasingly recognized that obesity may interact with genetic risk factors, notably *APOE* $\varepsilon4$ (Jones and Rebeck, 2018; Mole et al., 2020; Zade et al., 2013). Indeed, here we observed interaction effects between *APOE* and WHR on the size/complexity of the hippocampal formation. While all obese individuals showed reduced size/complexity, this effect was only significant for *APOE* $\varepsilon4$ non-carriers ($p < 0.001$) but not for *APOE* $\varepsilon4$ carriers ($p = 0.1$) (Fig. 7). As can be seen in Fig. 7, *APOE* $\varepsilon4$ carriers did not show a significant obesity effect because size/complexity was attenuated in normal-weighted *APOE* $\varepsilon4$ carriers. Thus, central obesity appeared to be related to atrophy in the hippocampal formation regardless of an individual's *APOE* or FH status (as no effects of FH were present). However, *APOE* $\varepsilon4$ carriage alone appeared also to be associated with adverse effects on the hippocampus and these may have masked any metabolic and vascular benefits of a healthy WHR. Or expressed differently, keeping a healthy weight may not be sufficient to compensate for *APOE* $\varepsilon4$-driven hippocampal atrophy. These risk effects were present for data collapsed across all hippocampal subfields. There was no evidence for any subfield specific vulnerability to the impact of obesity and *APOE* although trends were observed for CA1, CA2/3 and DG but not the subiculum. Future larger studies are required to clarify whether these regions are particularly susceptible to obesity and *APOE* $\varepsilon4$ related tissue changes and why this may be.

A previous analysis of data from the Framingham Offspring cohort also highlighted complex synergistic effects between *APOE* and obesity (Zade et al., 2013). They found several *APOE*-related modifications of correlations between individual differences in WHR on one hand and brain structure and cognition on the other. For instance, *APOE* $\varepsilon4$ carriers showed stronger negative relationships between WHR and executive and memory functions as well as larger correlations between WHR and white matter hyperintensities. Interestingly, they also reported a stronger correlation between WHR and frontal brain volume for *APOE* $\varepsilon4$ non-carriers similar to our observations here.

In addition, it is likely that obesity effects will be modulated by other polygenic risk factors than *APOE* $\varepsilon4$ (Woo and Reifman, 2018). While the CARDS sample was too small to quantify AD and/or obesity-related polygenic risk hazards (Escott-Price et al., 2014; Escott-Price et al., 2015), we included family history of dementia as a variable that captures environmental and genetic risk factors beyond *APOE* $\varepsilon4$. In the present analysis of hippocampal microstructure, we did not find any effect of FH, but previously we observed widespread interaction effects between *APOE*, FH, and WHR on white matter microstructure, that were most pronounced in the right parahippocampal cingulum (Mole et al., 2020). More specifically, *APOE* $\varepsilon4$ carriers with a positive FH, showed obesity-related reductions in apparent myelin MPF while no effects were observed for individuals without a FH. These risk-effects on apparent myelin were moderated by hypertension and inflammation-related blood markers (Mole et al., 2020).

The precise nature of these complex synergistic effects between obesity and *APOE* $\varepsilon4$ remain elusive and require further investigation. A recent animal study (Jones et al., 2021) points to inflammation and neuronal plasticity mechanisms underpinning interaction effects between obesity and *APOE* genotype. In this study, a high-fat diet increased gliosis and immediate-early gene expression only in *APOE* $\varepsilon3$ but not *APOE* $\varepsilon4$ knock-in mice. This suggested early dysregulation of adaptive inflammatory mechanisms in *APOE* $\varepsilon4$ mice that may make the brain more vulnerable to insults and damage in the long run. In addition, *APOE* $\varepsilon4$ is also known to lead to changes in glucose, insulin, and lipid metabolism and altered beta-amyloid production (Jones and Rebeck, 2018; Jones et al., 2019). Together, these findings suggest that *APOE* $\varepsilon4$ and obesity lead to metabolic alterations, including inflammatory processes, and may adversely interact with each other and with other genetic factors on brain structure and function. We propose that interaction effects between *APOE* $\varepsilon4$ and obesity on the hippocampal formation may increase that region's vulnerability to subsequent neurodegeneration.

The effects of risk on the hippocampal formation were observed while accounting for age and sex and interaction effects between WHR and *APOE* were only present for the size/complexity component. In contrast, aging was associated with a non-linear inverted U-shaped curve of the myelin/neurite packing component akin to the trajectory of white matter microstructure across the lifespan in humans and rhesus monkeys (Bartzokis et al., 2010; Kubicki et al., 2019; Slater et al., 2019; Yeatman et al., 2014). Myelin/neurite packing increased between the thirties and fourties seconds, when it peaked, remained relatively stable in the fifties and sixties and declined in the seventies (Fig. 5A). Age effects were present in all four subfields of the hippocampal formation, that is, CA1, CA2/3, DG, and subiculum. We propose that this observed age trajectory in the myelin/neurite packing component most likely reflects the maturation of white matter pathways within the hippocampal formation, such as the perforant path, mossy fiber, and Schaffer collateral pathways (Zeineh et al., 2017). Indeed, age-related differences in the myelin basic protein (MBP) expression were found in the CA1, CA2/3 and DG regions of gerbils such that white matter fibers of the perforant pathway, the mossy fibers and Schaffer collaterals were reduced in older relative to younger gerbils (Ahn et al., 2017) Our findings accord with a study (Douaud et al., 2014) that employed a data-driven analysis of gray matter structural variation and identified a brain network comprising prefrontal, intraparietal, posterior cingulate, and medial temporal lobe regions whose lifespan pattern mirrored brain development and age-related degeneration. The hippocampus forms part of this network which matures during adolescence and young adulthood into midlife and shows heightened vulnerability to accelerated neurodegeneration in older age (Douaud et al. 2014). As we did not observe any age-related differences in the size/complexity and metabolic components, we propose that hippocampal changes across midlife and early older age may be primarily driven by changes in white matter myelin and neurite packing rather than a loss of neurons and synapses.

Finally, we tested for the effects of risk factors on cognitive performance and explored the relationship between cognitive performance and hippocampal subfield macro- and microstructure. The dimensionality of the cognitive data was reduced to four components reflecting verbal and visual episodic memory as well as spatial navigation first move latencies and path length. We did not observe any risk effects on cognitive components. Additional analysis of risk factors on individual cognitive measurements did not reveal any risk effects either (*APOE:* $p = 0.5$, FH: $p = 0.6$, WHR: $p = 0.3$). This may suggest that risk-related macro- and microstructural tissue changes in the hippocampal formation precede any cognitive impairment and/or were too subtle to induce any functional impairments in this sample of cognitively healthy adults. In contrast, age was associated with larger latencies in the spatial navigation task due to older people taking longer to plan and initiate their first move in the virtual water maze. In addition, females performed better in the verbal recall test than males (Metzler-Baddeley et al., 2019a).

With regards to brain-cognition relationships we observed dissociations between left and right hemisphere contributions to verbal and visual recall. While verbal recall was predicted by microstructural differences in left CA1 and right DG, visual recall was only predicted by macro- and microstructural differences in right-lateralized CA1 and CA2/3 regions. This pattern of dissociations accords with previous evidence from epilepsy patients that verbal and visual episodic memory rely more on the left and right medial temporal lobes, respectively (Kaplan et al., 1994; Wagner et al., 2009).

Furthermore, we also observed functional dissociations between the subiculum and CA fields and DG. Episodic memory performance relies on the ability to complete as well as separate patterns, with CA regions, notably CA3, playing an important role in pattern completion and DG in pattern separation (Baker et al., 2016; Keinath et al., 2020; Pilly et al., 2018; Poli et al., 2018). Thus, we observed contributions from CA fields and DG to both visual and verbal recall performance. In contrast, microstructural differences in the subiculum were predictive of path length performance in the spatial navigation task. This finding accords with evidence that the subiculum is crucially involved in the representation of space and displays boundary-dependent neural activity (Lee et al., 2018; O'Mara, 2005). Thus, the here observed pattern of specific associations between hippocampal subfields and cognitive performance provides support for the dissociation between subicular representation of space involved in environmental navigation and episodic memory function mediated by CA and DG regions in the human hippocampus. These findings also highlight the possibility that, although risk factors had no apparent impact on cognition in the current study, they may predispose an individual for future episodic memory and navigational deficits.

In summary, we provide novel evidence for dissociations between age and age-independent risk effects on hippocampal subfield macro- and microstructure. Non-linear age effects in myelin/neurite packing were observed in all subfields of the hippocampal formation. Central obesity was associated with reductions in myelin/neurite packing and size/complexity across all subfields, with *APOE* genotype modifying the effects of obesity on size/complexity. Notably, *APOE* $\varepsilon 4$ carriers did not seem to benefit of a healthy Waist-Hip-Ratio as much as non-carriers. Age and sex were significantly related to performance differences in spatial navigation and recall but no effects of risk factors on cognition were present. We also provide evidence for dissociations between contributions of the subiculum to spatial navigation and of CA and DG regions to episodic memory performance as well as of left-right lateralization effects on verbal and visual recall. It remains to be determined if the observed risk-related hippocampal macro- and microstructural differences may precede any future cognitive decline.

Author contributions

CM-B: conceptualization, methodology, formal analysis, writing – original draft preparation, writing – review & editing, visualization, project administration, funding acquisition; BMC & PAG: formal analysis and writing of manuscript, RS: Resources & Analysis, JPA, SV: Writing – Review & Editing.

Disclosure statement

The authors declare no competing financial and/or non-financial interests.

Acknowledgements

This research was funded by a Research Fellowship awarded to CM-B from the Alzheimer's Society UK and BRACE Alzheimer's Research Charity (grant ref: 208). JPA is supported by the Wellcome Trust (grant 103722/Z14/Z) and BMC and SDV's contribution was supported by Wellcome Trust Senior Research Fellowship awarded to SDV (212273/Z/18/Z). The authors would like to thank Jilu Mole, Erika Leonaviciute, Fabrizio Fasano, John Evans, Peter Hobden and Sonya Foley-Bozorgzad for their assistance with MRI data acquisition and processing. The authors would also like to thank Derek A. Hamilton and Adam Hampshire for providing the virtual Morris water maze and Cambridge Brain Sciences battery tasks, Rosie Dwyer, Samantha Collins, Abbie Stark, and Emma Blenkinsop for their assistance with the collection and scoring of the cognitive and health data, and Rhodri Thomas for assistance with the *APOE* genotyping of the saliva samples.

References

Adler, D.H., Wisse, L.E.M., Ittyerah, R., Pluta, J.B., Ding, S.L., Xie, L., Wang, J., Kadivar, S., Robinson, J.L., Schuck, T., Trojanowski, J.Q., Grossman, M., Detre, J.A., Elliott, M.A., Toledo, J.B., Liu, W., Pickup, S., Miller, M.I., Das, S.R., Wolk, D.A., Yushkevich, P.A., 2018. Characterizing the human hippocampus in aging and Alzheimer's disease using a computational atlas derived from ex vivo MRI and histology. Proc Natl Acad Sci U S A 115 (16), 4252–4257.

Ahn, J.H., Lee, T.K., Park, J.H., Cho, J.H., Kim, I.H., Lee, J.C., Hong, S., Jeon, Y.H., Kang, I.J., Lee, Y.J., Won, M.H., Lee, C.H., 2017. Age-dependent differences in myelin basic protein expression in the hippocampus of young, adult and aged gerbils. Lab Anim Res 33 (3), 237–243.

Alosco, M.L., Spitznagel, M.B., Strain, G., Devlin, M., Crosby, R.D., Mitchell, J.E., Gunstad, J., 2014. Family history of Alzheimer's disease limits improvement in cognitive function after bariatric surgery. SAGE Open Med 2, 2050312114539477.

Anan, F., Masaki, T., Shimomura, T., Fujiki, M., Umeno, Y., Eshima, N., Saikawa, T., Yoshimatsu, H., 2010. Abdominal visceral fat accumulation is associated with hippocampus volume in non-dementia patients with type 2 diabetes mellitus. Neuroimage 49 (1), 57–62.

Angelopoulou, E., Paudel, Y.N., Papageorgiou, S.G., Piperi, C., 2021. APOE genotype and Alzheimer's disease: the influence of lifestyle and environmental factors. ACS Chem Neurosci 12 (15), 2749–2764.

Arnoldussen, I.A., Kiliaan, A.J., Gustafson, D.R., 2014. Obesity and dementia: adipokines interact with the brain. Eur Neuropsychopharmacol 24 (12), 1982–1999.

Baker, S., Vieweg, P., Gao, F., Gilboa, A., Wolbers, T., Black, S.E., Rosenbaum, R.S., 2016. The human dentate gyrus plays a necessary role in discriminating new memories. Curr Biol 26 (19), 2629–2634.

Bartzokis, G., Lu, P.H., Tingus, K., Mendez, M.F., Richard, A., Peters, D.G., Oluwadara, B., Barrall, K.A., Finn, J.P., Villablanca, P., Thompson, P.M., Mintz, J., 2010. Lifespan trajectory of myelin integrity and maximum motor speed. Neurobiol Aging 31 (9), 1554–1562.

Beard, J., Officer, A., Cassels, A., 2016. The world report on ageing and health. The Gerontologist 56 (2), 163–166.

Benes, F.M., Turtle, M., Khan, Y., Farol, P., 1994. Myelination of a key relay zone in the hippocampal formation occurs in the human brain during childhood, adolescence, and adulthood. Arch Gen Psychiatry 51 (6), 477–484.

Benjamini, Y., Hochberg, Y., 1995. Controlling the false discovery rate: a practical and powerful approach to multiple testing. J Royal Stat Soc B 57, 289–300.

Beydoun, M.A., Beydoun, H.A., Wang, Y., 2008. Obesity and central obesity as risk factors for incident dementia and its subtypes: a systematic review and meta–analysis. Obes Rev 9 (3), 204–218.

Bourbon-Teles, J., Bells, S., Jones, D.K., Coulthard, E., Rosser, A., Metzler-Baddeley, C., 2017. Myelin breakdown in human Huntington's disease: Multi-modal evidence from diffusion MRI and quantitative magnetization transfer. Neuroscience 403, 79–92.

Boyle, R., Knight, S.P., De Looze, C., Carey, D., Scarlett, S., Stern, Y., Robertson, I.H., Kenny, R.A., Whelan, R., 2021. Verbal intelligence is a more robust cross-sectional measure of cognitive reserve than level of education in healthy older adults. Alzheimers Res Ther 13 (1), 128.

Brown, T.I., Hasselmo, M.E., Stern, C.E., 2014. A high-resolution study of hippocampal and medial temporal lobe correlates of spatial context and prospective overlapping route memory. Hippocampus 24 (7), 819–839.

Businaro, R., Corsi, M., Asprino, R., Di Lorenzo, C., Laskin, D., Corbo, R.M., Ricci, S., Pinto, A., 2018. Modulation of Inflammation as a way of delaying Alzheimer's disease progression: the diet's role. Curr Alzheimer Res 15 (4), 363–380.

Callaghan, M.F., Helms, G., Lutti, A., Mohammadi, S., Weiskopf, N., 2015. A general linear relaxometry model of R1 using imaging data. Magn Reson Med 73 (3), 1309–1314.

Cattell, R.B., 1952. Factor analysis. Harper, New York.

Ceckler, T., Wolff, S., Yip, V., Balaban, R., 1992. Dynamic and chemical factors affecting water proton relaxation by macromolecules. J Magn Reson 637–645.

Cercignani, M., Alexander, D.C., 2006. Optimal acquisition schemes for in vivo quantitative magnetization transfer MRI. Magn Reson Med 56 (4), 803–810.

Chai, A.B., Lam, H.H.J., Kockx, M., Gelissen, I.C., 2021. Apolipoprotein E isoform-dependent effects on the processing of Alzheimer's amyloid-β. Biochim Biophys Acta Mol Cell Biol Lipids 1866 (9), 158980.

Chamberland, M., Raven, E.P., Genc, S., Duffy, K., Descoteaux, M., Parker, G.D., Tax, C.M.W., Jones, D.K., 2019. Dimensionality reduction of diffusion MRI measures for improved tractometry of the human brain. Neuroimage 200, 89–100.

Chan, D., Gallaher, L.M., Moodley, K., Minati, L., Burgess, N., Hartley, T., 2016. The 4 mountains test: a short test of spatial memory with high sensitivity for the diagnosis of pre-dementia Alzheimer's disease. J Vis Exp 116 (116), e54454.

Chuang, Y.F., An, Y., Bilgel, M., Wong, D.F., Troncoso, J.C., O'Brien, R.J., Breitner, J.C., Ferruci, L., Resnick, S.M., Thambisetty, M., 2016. Midlife adiposity predicts earlier onset of Alzheimer's dementia, neuropathology and presymptomatic cerebral amyloid accumulation. Mol Psychiatry 21 (7), 910–915.

Coad, B.M., Craig, E., Louch, R., Aggleton, J.P., Vann, S.D., Metzler-Baddeley, C., 2020. Precommissural and postcommissural fornix microstructure in healthy aging and cognition. Brain Neurosci Adv 4, 2398212819899316.

Colgan, N., Siow, B., O'Callaghan, J.M., Harrison, I.F., Wells, J.A., Holmes, H.E., Ismail, O., Richardson, S., Alexander, D.C., Collins, E.C., Fisher, E.M., Johnson, R., Schwarz, A.J., Ahmed, Z., O'Neill, M.J., Murray, T.K., Zhang, H., Lythgoe, M.F., 2016. Application of neurite orientation dispersion and density imaging (NODDI) to a tau pathology model of Alzheimer's disease. Neuroimage 125, 739–744.

Colon-Perez, L.M., Ibanez, K.R., Suarez, M., Torroella, K., Acuna, K., Ofori, E., Levites, Y., Vaillancourt, D.E., Golde, T.E., Chakrabarty, P., Febo, M., 2019. Neurite orientation dispersion and density imaging reveals white matter and hippocampal microstructure changes produced by Interleukin-6 in the TgCRND8 mouse model of amyloidosis. Neuroimage 202, 116138.

Cox, A.J., West, N.P., Cripps, A.W., 2015. Obesity, inflammation, and the gut microbiota. Lancet Diabetes Endocrinol 3 (3), 207–215.

Daducci, A., Canales-Rodríguez, E.J., Zhang, H., Dyrby, T.B., Alexander, D.C., Thiran, J.P., 2015. Accelerated microstructure imaging via convex optimization (AMICO) from diffusion MRI data. Neuroimage 105, 32–44.

Daugherty, A.M., Bender, A.R., Raz, N., Ofen, N., 2016. Age differences in hippocampal subfield volumes from childhood to late adulthood. Hippocampus 26 (2), 220–228.

de Flores, R., La Joie, R., Chételat, G., 2015a. Structural imaging of hippocampal subfields in healthy aging and Alzheimer's disease. Neuroscience 309, 29–50.

de Flores, R., La Joie, R., Landeau, B., Perrotin, A., Mezenge, F., de La Sayette, V., Eustache, F., Desgranges, B., Chetelat, G., 2015b. Effects of age and Alzheimer's disease on hippocampal subfields: comparison between manual and FreeSurfer volumetry. Hum Brain Mapp 36 (2), 463–474.

Dekkers, I.A., Jansen, P.R., Lamb, H.J., 2019. Obesity, brain volume, and white matter microstructure at MRI: a cross-sectional UK biobank study. Radiology 292, 270.

Dickstein, D.L., Weaver, C.M., Luebke, J.I., Hof, P.R., 2013. Dendritic spine changes associated with normal aging. Neuroscience 251, 21–32.

DiStefano, C., Zhu, M., Mindrila, D., 2009. Understanding and using factor scores: considerations for the applied researcher. Pract Assess Res Eval 14, 1–14.

Dommermuth, R., Ewing, K., 2018. Metabolic syndrome: systems thinking in heart disease. Prim Care 45 (1), 109–129.

Donix, M., Burggren, A.C., Suthana, N.A., Siddarth, P., Ekstrom, A.D., Krupa, A.K., Jones, M., Martin-Harris, L., Ercoli, L.M., Miller, K.J., Small, G.W., Bookheimer, S.Y., 2010. Family history of Alzheimer's disease and hippocampal structure in healthy people. Am J Psychiatry 167 (11), 1399–1406.

Douaud, G., Groves, A.R., Tamnes, C.K., Westlye, L.T., Duff, E.P., Engvig, A., Walhovd, K.B., James, A., Gass, A., Monsch, A.U., Matthews, P.M., Fjell, A.M., Smith, S.M., Johansen-Berg, H., 2014. A common brain network links development, aging, and vulnerability to disease. Proc Natl Acad Sci U S A 111 (49), 17648–17653.

Dounavi, M.E., Mak, E., Wells, K., Ritchie, K., Ritchie, C.W., Su, L., O' Brien, J.T., 2020. Volumetric alterations in the hippocampal subfields of subjects at increased risk of dementia. Neurobiol Aging 91, 36–44.

Eng, J., Ceckler, T.L., Balaban, R.S., 1991. Quantitative 1H magnetization transfer imaging in vivo. Magn Reson Med 17 (2), 304–314.

Escott-Price, V., Bellenguez, C., Wang, L.S., Choi, S.H., Harold, D., Jones, L., Holmans, P., Gerrish, A., Vedernikov, A., Richards, A., DeStefano, A.L., Lambert, J.C., Ibrahim-Verbaas, C.A., Naj, A.C., Sims, R., Jun, G., Bis, J.C., Beecham, G.W., Grenier-Boley, B., Russo, G., Thornton-Wells, T.A., Denning, N., Smith, A.V., Chouraki, V., Thomas, C., Ikram, M.A., Zelenika, D., Vardarajan, B.N., Kamatani, Y., Lin, C.F., Schmidt, H., Kunkle, B., Dunstan, M.L., Vronskaya, M., Johnson, A.D., Ruiz, A., Bihoreau, M.T., Reitz, C., Pasquier, F., Hollingworth, P., Hanon, O., Fitzpatrick, A.L., Buxbaum, J.D., Campion, D., Crane, P.K., Baldwin, C., Becker, T., Gudnason, V., Cruchaga, C., Craig, D., Amin, N., Berr, C., Lopez, O.L., De Jager, P.L., Deramecourt, V., Johnston, J.A., Evans, D., Lovestone, S., Letenneur, L., Hernández, I., Rubinsztein, D.C., Eiriksdottir, G., Sleegers, K., Goate, A.M., Fiévet, N., Huentelman, M.J., Gill, M., Brown, K., Kamboh, M.I., Keller, L., Barberger–Gateau, P., McGuinness, B., Larson, E.B., Myers, A.J., Dufouil, C., Todd, S., Wallon, D., Love, S., Rogaeva, E., Gallacher, J., George-Hyslop, P.S., Clarimon, J., Lleo, A., Bayer, A., Tsuang, D.W., Yu, L., Tsolaki, M., Bossù, P., Spalletta, G., Proitsi, P., Collinge, J., Sorbi, S., Garcia, F.S., Fox, N.C., Hardy, J., Naranjo, M.C., Bosco, P., Clarke, R., Brayne, C., Galimberti, D., Scarpini, E., Bonuccelli, U., Mancuso, M., Siciliano, G., Moebus, S., Mecocci, P., Zompo, M.D., Maier, W., Hampel, H., Pilotto, A., Frank-García, A., Panza, F., Solfrizzi, V., Caffarra, P., Nacmias, B., Perry, W., Mayhaus, M., Lannfelt, L., Hakonarson, H., Pichler, S., Carrasquillo, M.M., Ingelsson, M., Beekly, D., Alvarez, V., Zou, F., Valladares, O., Younkin, S.G., Coto, E., Hamilton-Nelson, K.L., Gu, W., Razquin, C., Pastor, P., Mateo, I., Owen, M.J., Faber, K.M., Jonsson, P.V., Combarros, O., O'Donovan, M.C., Cantwell, L.B., Soininen, H., Blacker, D., Mead, S., Mosley, T.H., Bennett, D.A., Harris, T.B., Fratiglioni, L., Holmes, C., de Bruijn, R.F., Passmore, P., Montine, T.J., Bettens, K., Rotter, J.I., Brice, A., Morgan, K., Foroud, T.M., Kukull, W.A., Hannequin, D., Powell, J.F., Nalls, M.A., Ritchie, K., Lunetta, K.L., Kauwe, J.S., Boerwinkle, E., Riemenschneider, M., Boada, M., Hiltunen, M., Martin, E.R., Schmidt, R., Rujescu, D., Dartigues, J.F., Mayeux, R., Tzourio, C., Hofman, A., Nöthen, M.M., Graff, C., Psaty, B.M., Haines, J.L., Lathrop, M., Pericak-Vance, M.A., Launer, L.J., Van Broeckhoven, C., Farrer, L.A., van Duijn, C.M., Ramirez, A., Seshadri, S., Schellenberg, G.D., Amouyel, P., Williams, J.Consortium, U.K.B.E., (CHS), C.H.S., 2014. Gene-wide analysis detects two new susceptibility genes for Alzheimer's disease. PLoS One 9 (2), e94661.

Escott-Price, V., Sims, R., Bannister, C., Harold, D., Vronskaya, M., Majounie, E., Badarinarayan, N., Morgan, K., Passmore, P., Holmes, C., Powell, J., Brayne, C., Gill, M., Mead, S., Goate, A., Cruchaga, C., Lambert, J.C., van Duijn, C., Maier, W., Ramirez, A., Holmans, P., Jones, L., Hardy, J., Seshadri, S., Schellenberg, G.D., Amouyel, P., Williams, J.GERAD/PERADES, consortia, I., 2015. Common polygenic variation enhances risk prediction for Alzheimer's disease. Brain 138 (Pt 12), 3673–3684.

Feringa, F.M., van der Kant, R., 2021. Cholesterol and Alzheimer's disease; from risk genes to pathological effects. Front Aging Neurosci 13, 690372.

Fischl, B., 2012. FreeSurfer. Neuroimage 62 (2), 774–781.

Flood, D.G., Buell, S.J., Defiore, C.H., Horwitz, G.J., Coleman, P.D., 1985. Age-related dendritic growth in dentate gyrus of human brain is followed by regression in the 'oldest old'. Brain Res 345 (2), 366–368.

Flood, D.G., Buell, S.J., Horwitz, G.J., Coleman, P.D., 1987. Dendritic extent in human dentate gyrus granule cells in normal aging and senile dementia. Brain Res 402 (2), 205–216.

Folstein, M., Folstein, S., McHugh, P., 1975. "Mini-mental state". A practical method for grading the cognitive state of patients for the clinician. J Psychiatr Res 12, 189–198.

Geeraert, B.L., Chamberland, M., Lebel, R.M., Lebel, C., 2020. Multimodal principal component analysis to identify major features of white matter structure and links to reading. PLoS One 15 (8), e0233244.

Geurts, J.J., Bö, L., Roosendaal, S.D., Hazes, T., Daniëls, R., Barkhof, F., Witter, M.P., Huitinga, I., van der Valk, P., 2007. Extensive hippocampal demyelination in multiple sclerosis. J Neuropathol Exp Neurol 66 (9), 819–827.

Giulietti, G., Bozzali, M., Figura, V., Spanò, B., Perri, R., Marra, C., Lacidogna, G., Giubilei, F., Caltagirone, C., Cercignani, M., 2012. Quantitative magnetization transfer provides information complementary to grey matter atrophy in Alzheimer's disease brains. Neuroimage 59 (2), 1114–1122.

Guillemot-Legris, O., Muccioli, G.G., 2017. Obesity-Induced neuroinflammation: beyond the hypothalamus. Trends Neurosci 40 (4), 237–253.
Hamilton, D., Driscoll, I., Sutherland, R., 2002. Human place learning in a virtual Morris water task: some important constraints on the flexibility of place navigation. Behav Brain Res 129 (1–2), 159–170.
Hampshire, A., Highfield, R.R., Parkin, B.L., Owen, A.M., 2012. Fractionating human intelligence. Neuron 76 (6), 1225–1237.
Hao, S., Dey, A., Yu, X., Stranahan, A.M., 2016. Dietary obesity reversibly induces synaptic stripping by microglia and impairs hippocampal plasticity. Brain Behav Immun 51, 230–239.
Harrison, N.A., Cooper, E., Dowell, N.G., Keramida, G., Voon, V., Critchley, H.D., Cercignani, M., 2015. Quantitative magnetization transfer imaging as a biomarker for effects of systemic inflammation on the brain. Biol Psychiatry 78 (1), 49–57.
Hartley, M., Taylor, N., Taylor, J., 2005. Subfield variations in hippocampal processing-components of a spatial navigation system. Neural Netw 18 (5-6), 611–619.
Henkelman, R.M., Huang, X., Xiang, Q.S., Stanisz, G.J., Swanson, S.D., Bronskill, M.J., 1993. Quantitative interpretation of magnetization transfer. Magn Reson Med 29 (6), 759–766.
Henkelman, R.M., Stanisz, G.J., Graham, S.J., 2001. Magnetization transfer in MRI: a review. NMR Biomed 14 (2), 57–64.
Hoang, T.H., Aliane, V., Manahan-Vaughan, D., 2018. Novel encoding and updating of positional, or directional, spatial cues are processed by distinct hippocampal subfields: Evidence for parallel information processing and the "what" stream. Hippocampus 28 (5), 315–326.
IBM, 2011. SPSS Statistics, Version 20.0. IBM Corp., Armonk, NY.
Iglesias, J.E., Augustinack, J.C., Nguyen, K., Player, C.M., Player, A., Wright, M., Roy, N., Frosch, M.P., McKee, A.C., Wald, L.L., Fischl, B., Van Leemput, K., Initiative, A.s.D.N., 2015. A computational atlas of the hippocampal formation using ex vivo, ultra-high resolution MRI: Application to adaptive segmentation of in vivo MRI. Neuroimage 115, 117–137.
Irfanoglu, M.O., Walker, L., Sarlls, J., Marenco, S., Pierpaoli, C., 2012. Effects of image distortions originating from susceptibility variations and concomitant fields on diffusion MRI tractography results. Neuroimage 61 (1), 275–288.
Jack, C.R., Knopman, D.S., Jagust, W.J., Petersen, R.C., Weiner, M.W., Aisen, P.S., Shaw, L.M., Vemuri, P., Wiste, H.J., Weigand, S.D., Lesnick, T.G., Pankratz, V.S., Donohue, M.C., Trojanowski, J.Q., 2013. Tracking pathophysiological processes in Alzheimer's disease: an updated hypothetical model of dynamic biomarkers. Lancet Neurol 12 (2), 207–216.
Jenkinson, M., Beckmann, C.F., Behrens, T.E., Woolrich, M.W., Smith, S.M., 2012. FSL. Neuroimage 62 (2), 782–790.
Jezzard, P., Balaban, R.S., 1995. Correction for geometric distortion in echo planar images from B0 field variations. Magn Reson Med 34 (1), 65–73.
Johnson, S.C., Christian, B.T., Okonkwo, O.C., Oh, J.M., Harding, S., Xu, G., Hillmer, A.T., Wooten, D.W., Murali, D., Barnhart, T.E., Hall, L.T., Racine, A.M., Klunk, W.E., Mathis, C.A., Bendlin, B.B., Gallagher, C.L., Carlsson, C.M., Rowley, H.A., Hermann, B.P., Dowling, N.M., Asthana, S., Sager, M.A., 2014. Amyloid burden and neural function in people at risk for Alzheimer's Disease. Neurobiol Aging 35 (3), 576–584.
Jones, D.K., Horsfield, M.A., Simmons, A., 1999. Optimal strategies for measuring diffusion in anisotropic systems by magnetic resonance imaging. Magn Reson Med 42 (3), 515–525.
Jones, N.S., Rebeck, G.W., 2018. The synergistic effects of APOE genotype and obesity on Alzheimer's disease risk. Int J Mol Sci 20 (1), 63–74.
Jones, N.S., Watson, K.Q., Rebeck, G.W., 2019. Metabolic disturbances of a high-fat diet are dependent on APOE genotype and sex. eNeuro 6 (5), 1–11.
Jones, N.S., Watson, K.Q., Rebeck, G.W., 2021. High-fat diet increases gliosis and immediate early gene expression in APOE3 mice, but not APOE4 mice. J Neuroinflammation 18 (1), 214.
Kaplan, R.F., Meadows, M.E., Verfaellie, M., Kwan, E., Ehrenberg, B.L., Bromfield, E.B., Cohen, R.A., 1994. Lateralization of memory for the visual attributes of objects: evidence from the posterior cerebral artery amobarbital test. Neurology 44 (6), 1069–1073.
Keinath, A.T., Nieto-Posadas, A., Robinson, J.C., Brandon, M.P., 2020. DG-CA3 circuitry mediates hippocampal representations of latent information. Nat Commun 11 (1), 3026.
Kerchner, G.A., Berdnik, D., Shen, J.C., Bernstein, J.D., Fenesy, M.C., Deutsch, G.K., Wyss-Coray, T., Rutt, B.K., 2014. APOE ε4 worsens hippocampal CA1 apical neuropil atrophy and episodic memory. Neurology 82 (8), 691–697.
Khan, N.A., Baym, C.L., Monti, J.M., Raine, L.B., Drollette, E.S., Scudder, M.R., Moore, R.D., Kramer, A.F., Hillman, C.H., Cohen, N.J., 2015. Central adiposity is negatively associated with hippocampal-dependent relational memory among overweight and obese children. J Pediatr 166 (2), 302–308 e301.
Khan, W., Westman, E., Jones, N., Wahlund, L.O., Mecocci, P., Vellas, B., Tsolaki, M., Kłoszewska, I., Soininen, H., Spenger, C., Lovestone, S., Muehlboeck, J.S., Simmons, A.Initiative, A.c.a.f.t.A.s.D.N., 2015. Automated hippocampal subfield measures as predictors of conversion from mild cognitive impairment to Alzheimer's disease in two independent cohorts. Brain Topogr 28 (5), 746–759.
Klein, S., Staring, M., Murphy, K., Viergever, M.A., Pluim, J.P., 2010. elastix: a toolbox for intensity-based medical image registration. IEEE Trans Med Imaging 29 (1), 196–205.
Knight, M.J., McCann, B., Kauppinen, R.A., Coulthard, E.J., 2016. Magnetic resonance imaging to detect early molecular and cellular changes in alzheimer's disease. Front Aging Neurosci 8, 139.
Knight, M.J., Wearn, A., Coulthard, E., Kauppinen, R.A., 2019. T2 relaxometry and diffusion tensor indices of the hippocampus and entorhinal cortex improve sensitivity and specificity of MRI to detect amnestic mild cognitive impairment and Alzheimer's disease dementia. J Magn Reson Imaging. 49 (2), 445–455.
Kodiweera, C., Alexander, A.L., Harezlak, J., McAllister, T.W., Wu, Y.C., 2016. Age effects and sex differences in human brain white matter of young to middle-aged adults: A DTI, NODDI, and q-space study. Neuroimage. 128, 180–192.
Koster, A., Murphy, R.A., Eiriksdottir, G., Aspelund, T., Sigurdsson, S., Lang, T.F., Gudnason, V., Launer, L.J., Harris, T.B., 2015. Fat distribution and mortality: the AGES-Reykjavik Study. Obesity (Silver Spring). 23 (4), 893–897.
Koster, A., Schaap, L.A., 2015. The effect of type 2 diabetes on body composition of older adults. Clin Geriatr Med. 31 (1), 41–49 vii-viii.
Koster, A., Stenholm, S., Alley, D.E., Kim, L.J., Simonsick, E.M., Kanaya, A.M., Visser, M., Houston, D.K., Nicklas, B.J., Tylavsky, F.A., Satterfield, S., Goodpaster, B.H., Ferrucci, L., Harris, T.B., Study, H.A., 2010. Body fat distribution and inflammation among obese older adults with and without metabolic syndrome. Obesity (Silver Spring). 18 (12), 2354–2361.
Koutsodendris, N., Nelson, M.R., Rao, A., Huang, Y., 2021. Apolipoprotein E and Alzheimer's disease: findings, hypotheses, and potential mechanisms. Annu Rev Pathol 17, 73–99.
Kubicki, M., Baxi, M., Pasternak, O., Tang, Y., Karmacharya, S., Chunga, N., Lyall, A.E., Rathi, Y., Eckbo, R., Bouix, S., Mortazavi, F., Papadimitriou, G., Shenton, M.E., Westin, C.F., Killiany, R., Makris, N., Rosene, D.L., 2019. Lifespan trajectories of white matter changes in rhesus monkeys. Cereb Cortex. 29 (4), 1584–1593.
Kyle, C.T., Smuda, D.N., Hassan, A.S., Ekstrom, A.D., 2015. Roles of human hippocampal subfields in retrieval of spatial and temporal context. Behav Brain Res. 278, 549–558.
La Joie, R., Fouquet, M., Mezenge, F., Landeau, B., Villain, N., Mevel, K., Pelerin, A., Eustache, F., Desgranges, B., Chetelat, G., 2010. Differential effect of age on hippocampal subfields assessed using a new high-resolution 3T MR sequence. Neuroimage. 53 (2), 506–514.
Lakens, D., 2014. Performing high-powered studies efficiently with sequential analyses: sequential analyses. Eur J Soc Psychol. 44 (7), 701–710.
Lampe, L., Zhang, R., Beyer, F., Huhn, S., Kharabian Masouleh, S., Preusser, S., Bazin, P.L., Schroeter, M.L., Villringer, A., Witte, A.V., 2019. Visceral obesity relates to deep white matter hyperintensities via inflammation. Ann Neurol. 85 (2), 194–203.
Lee, S.A., Miller, J.F., Watrous, A.J., Sperling, M.R., Sharan, A., Worrell, G.A., Berry, B.M., Aronson, J.P., Davis, K.A., Gross, R.E., Lega, B., Sheth, S., Das, S.R., Stein, J.M., Gorniak, R., Rizzuto, D.S., Jacobs, J., 2018. Electrophysiological Signatures of Spatial Boundaries in the Human Subiculum. J Neurosci. 38 (13), 3265–3272.
Leemans, A, Jeurissen, B, Sijbers, J, DK, J., 2009. ExploreDTI: a graphical toolbox for processing, analyzing, and visualizing diffusion MR data. In: 17th Annual Meeting of Intl Soc Mag Reson Med. Hawaii, USA, p. 3537.
Leemans, A., Jones, D.K., 2009. The B-matrix must be rotated when correcting for subject motion in DTI data. Magn Reson Med. 61 (6), 1336–1349.
Lindberg, O., Mårtensson, G., Stomrud, E., Palmqvist, S., Wahlund, L.O., Westman, E., Hansson, O., 2017. Atrophy of the posterior subiculum is associated with memory impairment, tau- and Aβ pathology in non-demented individuals. Front Aging Neurosci. 9, 306.
Liu, C.C., Kanekiyo, T., Xu, H., Bu, G., 2013. Apolipoprotein E and Alzheimer disease: risk, mechanisms and therapy. Nat Rev Neurol. 9 (2), 106–118.
Malykhin, N.V., Huang, Y., Hrybouski, S., Olsen, F., 2017. Differential vulnerability of hippocampal subfields and anteroposterior hippocampal subregions in healthy cognitive aging. Neurobiol Aging. 59, 121–134.
Menzler, K., Hamer, H.M., Mross, P., Rosenow, F., Deichmann, R., Wagner, M., Gracien, R.M., Doerfler, A., Bluemcke, I., Coras, R., Belke, M., Knake, S., 2021. Validation of automatic MRI hippocampal subfield segmentation by histopathological evaluation in patients with temporal lobe epilepsy. Seizure. 87, 94–102.
Metzler-Baddeley, C., Foley, S., de Santis, S., Charron, C., Hampshire, A., Caeyenberghs, K., Jones, D.K., 2017. Dynamics of white matter plasticity underlying working memory training: multimodal evidence from diffusion MRI and relaxometry. J Cogn Neurosci. 29 (9), 1509–1520.
Metzler-Baddeley, C., Mole, J., Leonaviciute, E., Sims, R., Kelso-Mitchell, A., Gidney, F., Fasano, F., Evans, J., Kidd, E., Ertefai, B., Jones, D., Baddeley, R., 2019a. Sex-specific effects of central adiposity and inflammatory markers on limbic microstructure. NeuroImage 793–803.
Metzler-Baddeley, C., Mole, J., Sims, R., Fasano, F., Evans, J., Jones, D., Aggleton, J., Baddeley, R., 2019b. Fornix white matter glia damage causes hippocampal gray matter damage during age-dependent limbic decline, Scientific Reports. Nature Publishing Group, p. 1060.
Mizutani, M., Sone, D., Sano, T., Kimura, Y., Maikusa, N., Shigemoto, Y., Goto, Y., Takao, M., Iwasaki, M., Matsuda, H., Sato, N., Saito, Y., 2021. Histopathological validation and clinical correlates of hippocampal subfield volumetry based on T2-weighted MRI in temporal lobe epilepsy with hippocampal sclerosis. Epilepsy Res. 177, 106759.
Mole, J., Fasano, F., Evans, J., Sims, R., Hamilton, D., Kidd, E., Metzler-Baddeley, C., 2020. Genetic risk of dementia modifies obesity effects on white matter myelin in cognitively healthy adults. Neurobiol Aging.
Mueller, K., Sacher, J., Arelin, K., Holiga, S., Kratzsch, J., Villringer, A., Schroeter, M.L., 2012. Overweight and obesity are associated with neuronal injury in the human cerebellum and hippocampus in young adults: a combined MRI, serum marker and gene expression study. Transl Psychiatry 2, e200.
Mueller, S.G., Schuff, N., Raptentsetsang, S., Elman, J., Weiner, M.W., 2008. Selective effect of Apo e4 on CA3 and dentate in normal aging and Alzheimer's disease using high resolution MRI at 4 T. Neuroimage 42 (1), 42–48.

Mueller, S.G., Weiner, M.W., 2009. Selective effect of age, Apo e4, and Alzheimer's disease on hippocampal subfields. Hippocampus 19 (6), 558–564.

Nazeri, A., Chakravarty, M.M., Rotenberg, D.J., Rajji, T.K., Rathi, Y., Michailovich, O.V., Voineskos, A.N., 2015. Functional consequences of neurite orientation dispersion and density in humans across the adult lifespan. J Neurosci. 35 (4), 1753–1762.

Nelson, H.E., 1991. The National Adult Reading Test-Revised (NART-R): Test manual. National Foundation for Educational Research-Nelson., Windsor, UK.

O'Mara, S., 2005. The subiculum: what it does, what it might do, and what neuroanatomy has yet to tell us. J Anat 207 (3), 271–282.

Owen, A.M., Hampshire, A., Grahn, J.A., Stenton, R., Dajani, S., Burns, A.S., Howard, R.J., Ballard, C.G., 2010. Putting brain training to the test. Nature 465 (7299), 775–778.

Pedditizi, E., Peters, R., Beckett, N., 2016. The risk of overweight/obesity in mid-life and late life for the development of dementia: a systematic review and meta–analysis of longitudinal studies. Age Ageing 45 (1), 14–21.

Penke, L., Muñoz Maniega, S., Murray, C., Gow, A.J., Hernández, M.C., Clayden, J.D., Starr, J.M., Wardlaw, J.M., Bastin, M.E., Deary, I.J., 2010. A general factor of brain white matter integrity predicts information processing speed in healthy older people. J Neurosci 30 (22), 7569–7574.

Pilly, P.K., Howard, M.D., Bhattacharyya, R., 2018. Modeling Contextual Modulation of Memory Associations in the Hippocampus. Front Hum Neurosci 12, 442.

Poli, D., Wheeler, B.C., DeMarse, T.B., Brewer, G.J., 2018. Pattern separation and completion of distinct axonal inputs transmitted via micro-tunnels between co-cultured hippocampal dentate, CA3, CA1 and entorhinal cortex networks. J Neural Eng 15 (4), 046009.

Profenno, L.A., Porsteinsson, A.P., Faraone, S.V., 2010. Meta-analysis of Alzheimer's disease risk with obesity, diabetes, and related disorders. Biol Psychiatry 67 (6), 505–512.

Ramani, A., Dalton, C., Miller, D.H., Tofts, P.S., Barker, G.J., 2002. Precise estimate of fundamental in-vivo MT parameters in human brain in clinically feasible times. Magn Reson Imaging 20 (10), 721–731.

Raz, N., 2001. Ageing and the brain. Encyclopedia of Life Sciences 1–6.

Raz, N., Daugherty, A.M., Bender, A.R., Dahle, C.L., Land, S., 2015. Volume of the hippocampal subfields in healthy adults: differential associations with age and a pro-inflammatory genetic variant. Brain Struct Funct. 220 (5), 2663–2674.

Reiter, K., Nielson, K.A., Durgerian, S., Woodard, J.L., Smith, J.C., Seidenberg, M., Kelly, D.A., Rao, S.M., 2017. Five-year longitudinal brain volume change in healthy elders at genetic risk for Alzheimer's disease. J Alzheimers Dis. 55 (4), 1363–1377.

Rey, A., 1941. L'examen psychologique dans les cas d'encephalopathie traumatique. Arch de Psychologie 28, 215–285.

Ricci, G., Pirillo, I., Tomassoni, D., Sirignano, A., Grappasonni, I., 2017. Metabolic syndrome, hypertension, and nervous system injury: epidemiological correlates. Clin Exp Hypertens. 39 (1), 8–16.

Schmidt, M., 1996. Rey Auditory and Verbal Learning Test. A handbook. Western Psychological Association, Los Angeles.

Schmierer, K., Tozer, D.J., Scaravilli, F., Altmann, D.R., Barker, G.J., Tofts, P.S., Miller, D.H., 2007. Quantitative magnetization transfer imaging in postmortem multiple sclerosis brain. J Magn Reson Imaging. 26 (1), 41–51.

Seiger, R., Hammerle, F.P., Godbersen, G.M., Reed, M.B., Spurny-Dworak, B., Handschuh, P., Klöbl, M., Unterholzner, J., Gryglewski, G., Vanicek, T., Lanzenberger, R., 2021. Comparison and reliability of hippocampal subfield segmentations within freesurfer utilizing T1- and T2-weighted multispectral MRI data. Front Neurosci. 15, 666000.

Seress, L., Gulyás, A.I., Ferrer, I., Tunon, T., Soriano, E., Freund, T.F., 1993. Distribution, morphological features, and synaptic connections of parvalbumin- and calbindin D28k-immunoreactive neurons in the human hippocampal formation. J Comp Neurol. 337 (2), 208–230.

Seress, L., Gulyás, A.I., Freund, T.F., 1992. Pyramidal neurons are immunoreactive for calbindin D28k in the CA1 subfield of the human hippocampus. Neurosci Lett. 138 (2), 257–260.

Seress, L., Léránth, C., Frotscher, M., 1994. Distribution of calbindin D28k immunoreactive cells and fibers in the monkey hippocampus, subicular complex and entorhinal cortex. A light and electron microscopic study. J Hirnforsch. 35 (4), 473–486.

Slater, D.A., Melie-Garcia, L., Preisig, M., Kherif, F., Lutti, A., Draganski, B., 2019. Evolution of white matter tract microstructure across the life span. Hum Brain Mapp. 40 (7), 2252–2268.

Sled, J.G., 2017. Modelling and interpretation of magnetization transfer imaging in the brain. Neuroimage 182, 128–135.

Spencer, S.J., D'Angelo, H., Soch, A., Watkins, L.R., Maier, S.F., Barrientos, R.M., 2017. High-fat diet and aging interact to produce neuroinflammation and impair hippocampal- and amygdalar-dependent memory. Neurobiol Aging. 58, 88–101.

Stranahan, A.M., 2015. Models and mechanisms for hippocampal dysfunction in obesity and diabetes. Neuroscience. 309, 125–139.

Tang, X., Cai, F., Ding, D.X., Zhang, L.L., Cai, X.Y., Fang, Q., 2018. Magnetic resonance imaging relaxation time in Alzheimer's disease. Brain Res Bull. 140, 176–189.

Tanzi, R.E., 2012. The genetics of Alzheimer disease. Cold Spring Harb Perspect Med. 2 (10), a006296.

Tardif, C.L., Devenyi, G.A., Amaral, R.S.C., Pelleieux, S., Poirier, J., Rosa-Neto, P., Breitner, J., Chakravarty, M.M., Group, P.-A.R., 2018. Regionally specific changes in the hippocampal circuitry accompany progression of cerebrospinal fluid biomarkers in preclinical Alzheimer's disease. Hum Brain Mapp. 39 (2), 971–984.

Tuch, D.S., Reese, T.G., Wiegell, M.R., Makris, N., Belliveau, J.W., Wedeen, V.J., 2002. High angular resolution diffusion imaging reveals intravoxel white matter fiber heterogeneity. Magn Reson Med. 48 (4), 577–582.

Uribe, C., Segura, B., Baggio, H.C., Campabadal, A., Abos, A., Compta, Y., Marti, M.J., Valldeoriola, F., Bargallo, N., Junque, C., 2018. Differential progression of regional hippocampal atrophy in aging and Parkinson's disease. Front Aging Neurosci. 10, 325.

Veldsman, M., Nobis, L., Alfaro-Almagro, F., Manohar, S., Husain, M., 2021. The human hippocampus and its subfield volumes across age, sex and APOE e4 status. Brain Commun. 3 (1), fcaa219.

Wagner, D.D., Sziklas, V., Garver, K.E., Jones-Gotman, M., 2009. Material-specific lateralization of working memory in the medial temporal lobe. Neuropsychologia. 47 (1), 112–122.

Whitmer, R.A., Gunderson, E.P., Quesenberry, C.P., Zhou, J., Yaffe, K., 2007. Body mass index in midlife and risk of Alzheimer disease and vascular dementia. Curr Alzheimer Res. 4 (2), 103–109.

Willette, A.A., Kapogiannis, D., 2015. Does the brain shrink as the waist expands? Ageing Res Rev. 20, 86–97.

Wisse, L.E., Biessels, G.J., Heringa, S.M., Kuijf, H.J., Koek, D.H., Luijten, P.R., Geerlings, M.I.Utrecht Vascular Cognitive Impairment Study, G., 2014. Hippocampal subfield volumes at 7T in early Alzheimer's disease and normal aging. Neurobiol Aging. 35 (9), 2039–2045.

Wolf, D., Fischer, F.U., de Flores, R., Chetelat, G., Fellgiebel, A., 2015. Differential associations of age with volume and microstructure of hippocampal subfields in healthy older adults. Hum Brain Mapp. 36 (10), 3819–3831.

Wolf, P.A., 2012. Contributions of the Framingham Heart Study to stroke and dementia epidemiologic research at 60 years. Arch Neurol. 69 (5), 567–571.

Woo, H.J., Reifman, J., 2018. Genetic interaction effects reveal lipid-metabolic and inflammatory pathways underlying common metabolic disease risks. BMC Med Genomics. 11 (1), 54.

World Health Organisation, 2008. Waist Circumference and Waist-Hip-Ratio: Report of a WHO expert consultation. World Health Organisation, Geneva.

Xu, W.L., Atti, A.R., Gatz, M., Pedersen, N.L., Johansson, B., Fratiglioni, L., 2011. Midlife overweight and obesity increase late-life dementia risk: a population-based twin study. Neurology. 76 (18), 1568–1574.

Yeatman, J.D., Wandell, B.A., Mezer, A.A., 2014. Lifespan maturation and degeneration of human brain white matter. Nat Commun. 5, 4932.

Yushkevich, P.A., Amaral, R.S., Augustinack, J.C., Bender, A.R., Bernstein, J.D., Boccardi, M., Bocchetta, M., Burggren, A.C., Carr, V.A., Chakravarty, M.M., Chetelat, G., Daugherty, A.M., Davachi, L., Ding, S.L., Ekstrom, A., Geerlings, M.I., Hassan, A., Huang, Y., Iglesias, J.E., La Joie, R., Kerchner, G.A., LaRocque, K.F., Libby, L.A., Malykhin, N., Mueller, S.G., Olsen, R.K., Palombo, D.J., Parekh, M.B., Pluta, J.B., Preston, A.R., Pruessner, J.C., Ranganath, C., Raz, N., Schlichting, M.L., Schoemaker, D., Singh, S., Stark, C.E., Suthana, N., Tompary, A., Turowski, M.M., Van Leemput, K., Wagner, A.D., Wang, L., Winterburn, J.L., Wisse, L.E., Yassa, M.A., Zeineh, M.M., Hippocampal Subfields, G., 2015a. Quantitative comparison of 21 protocols for labeling hippocampal subfields and parahippocampal subregions in in vivo MRI: towards a harmonized segmentation protocol. Neuroimage. 111, 526–541.

Yushkevich, P.A., Pluta, J.B., Wang, H., Xie, L., Ding, S.L., Gertje, E.C., Mancuso, L., Kliot, D., Das, S.R., Wolk, D.A., 2015b. Automated volumetry and regional thickness analysis of hippocampal subfields and medial temporal cortical structures in mild cognitive impairment. Hum Brain Mapp. 36 (1), 258–287.

Zade, D., Beiser, A., McGlinchey, R., Au, R., Seshadri, S., Palumbo, C., Wolf, P.A., DeCarli, C., Milberg, W., 2013. Apolipoprotein epsilon 4 allele modifies waist-to-hip ratio effects on cognition and brain structure. J Stroke Cerebrovasc Dis. 22 (2), 119–125.

Zeineh, M.M., Palomero-Gallagher, N., Axer, M., Gräßel, D., Goubran, M., Wree, A., Woods, R., Amunts, K., Zilles, K., 2017. Direct visualization and mapping of the spatial course of fiber tracts at microscopic resolution in the human hippocampus. Cereb Cortex. 27 (3), 1779–1794.

Zhang, H., Schneider, T., Wheeler-Kingshott, C.A., Alexander, D.C., 2012. NODDI: practical in vivo neurite orientation dispersion and density imaging of the human brain. Neuroimage. 61 (4), 1000–1016.